

1 **Challenges and Alternatives to Empirical Orthogonal Functions for Earth System Data**

2

3 Christine A. Shields¹, Derek DeSantis², Alexandra Jonko³, Jiwoo Lee⁴, Julie M. Caron¹, Adam S.

4 Phillips¹, John Fasullo¹

5

6 ¹NSF National Center for Atmospheric Research, Boulder, CO 80302, USA

7 ²Computer, Computational & Statistical Science Division, Los Alamos National Laboratory, Los

8 Alamos, NM 87545, USA

9 ³Earth and Environmental Sciences Division, Los Alamos National Laboratory, Los Alamos, NM 87545,

10 USA

11 ⁴Atmospheric, Earth, and Energy Division, Lawrence Livermore National Laboratory, Livermore, CA

12 94550, USA

13

14

15 Corresponding author: shields@ucar.edu

16

17

18

19

20

21

22

23

24

25 **Abstract**

26 Empirical Orthogonal Functions (EOFs) applied to gridded Earth system data enables users to diagnose
27 modes of variability with relative ease. Yet, many challenges to interpretation exist such that they must be
28 used with awareness and intention when applied to gridded climate data, especially with large ensembles.
29 Utilizing data from two different Earth system modelling large ensemble frameworks, the Energy
30 Exoscale Earth System Model (E3SM) and the Community Earth System Model (CESM), as well as
31 reanalysis data, common EOF pitfalls are summarized and discussed. Challenges include erroneous mode
32 swapping, sign flipping, and the temporal variability of the centers of action. For modes of variability
33 with similar contribution to variance, mode swapping is not uncommon. Sign flipping can occur with
34 almost any mode where the pattern is correct, but the sign is arbitrary. Although the variability of the
35 center of action is not necessarily problematic, it potentially complicates interpretation over multi-century
36 timescales. A wide variety of alternative methods to EOFs exist, but fitness-for-purpose must be
37 evaluated. Additionally, illustrations of alternative methods and examples of proper use are provided.
38 Alternative methods fit into three categories: EOF variants, linear methods, and multilinear methods are
39 provided.

40

41 **Key Words/Phrases**

42 Climate data, Earth system models, EOFs, PCA, Modes of variability

43

44

45 **Introduction**

46 Principal Component Analysis (PCA) is a widely used method for assessing gridded climate datasets.
47 Whether the data takes the form of reanalyses, observational products, or model output, understanding
48 Earth's climate and its variability often involves quantifying patterns of variability, disentangling them
49 from external forcing such as anthropogenic climate change, or simplifying predictions with the use of

50 linear inverse modelling¹. PCA is a commonly used approach which decomposes data into (1) spatial
51 patterns, referred to as Empirical Orthogonal Functions (EOFs) and (2) a time-varying principal
52 components (PC), representing the variation of the amplitudes of the EOFs over time. Although patterns
53 produced from geophysical data can be interpreted as physical variance patterns occurring naturally in the
54 Earth system, the data structures themselves are distinct from real physical processes. Patterns are defined
55 to be orthogonal and sorted by contributions to total variance, in a specified domain, temporally across the
56 dataset. EOF modes are uncorrelated with each other, in that the different patterns of variance may not
57 necessarily be related to each other^{2,3,4,5,6}. For example, a very common internal mode of climate
58 variability in the Northern Hemisphere is the Pacific North American Pattern (PNA), a storm track
59 pattern. In observations, the PNA is the leading EOF of interannual sea -level pressure (PSL) anomalies.
60 The second leading mode is the NPO (North Pacific Oscillation), an orthogonal pattern oriented as a
61 meridional dipole in contrast to the PNA, whose structure is primarily zonal. Reproducing these patterns
62 in observations is influenced by parametric choices such as time period and domain bounds. Reproducing
63 patterns in ensembles of climate models can be complicated further by orthogonal modes with similar
64 variance across the dataset, such that the ordering of the modes is inconsistent across individual
65 simulations. This is called mode-swapping. It has been documented in a number of papers^{5,7,8,9}, and can
66 have serious implications for interpretability of the dominant mode in both models and observations. The
67 purpose of this article is to, in one place, examine common pitfalls in PCA analysis when applying EOFs
68 and outline approaches for dealing with them. Our intent is *not* to describe dominant modes of
69 variability, nor to provide a deep-dive into PCA mathematics, but rather to utilize the novel opportunity
70 provided by large and multi-model ensembles to explore statistical aspects of EOF analysis. While EOF
71 analysis can also be applied to spatially non-gridded data, here, we limit our illustrations to spatially
72 gridded climate data. We acknowledge that some of these pitfalls are simply natural characteristics of the
73 method, rather than problems per se, however, challenges do arise when using EOFs to evaluate physical
74 patterns, and particularly multi-model comparisons and large ensemble studies. Throughout this article,
75 we intertwine discussion of EOFs, their modes, and respective physical interpretations, all together, to

76 frame PCA within the context of typical community practices. However, it is important to acknowledge
77 again that the data structures themselves are indeed distinct from the physical patterns, and it is our
78 interpretation of them that is the challenge. Further discussion can be found in Methods under
79 *Techniques: Standard EOF Computation*. We follow in the spirit of earlier literature, each aimed at
80 addressing specific aspects of the challenge^{5,8}. Lee et al. (2019)⁸ proposed applying common basis
81 functions (CBFs) to EOFs as a means of using observations to mitigate for pitfalls of PCA in evaluating
82 climate models. CBFs can correct for mode swapping, sign swapping (i.e, the arbitrarily assigned signs
83 of EOFs that are inconsistent with observations), and potentially misinterpretation related to mode center
84 of action variability. Although the application of CBF works well for historical simulations, it is not well-
85 suited for cases where the patterns of modes change, such as in past or future climates. Techniques
86 considered to be an alternative to EOFs and traditional PCA analysis include rotated EOFs (REOFs).
87 Rotated EOFs can address issues related to the production of potentially unphysical modes and mode
88 mixing, and have been explored in earlier work^{10,11}. Even using REOFs, however, some of the classic
89 problems, such as interpretability and geophysical pattern reliance on domain choice, still remain^{12,13}.
90 Many issues arise when analyzing climate model simulations, especially in large ensembles, which
91 consist of multiple simulations (>20) initialized with slightly different conditions but using identical
92 external climate forcings. Over the past decade, large ensembles have emerged as a critical and necessary
93 tool for disentangling natural and forced climate signals^{14,15}, in part, by benchmarking modes of
94 variability (MOV) internal noise^{16,17,18,19}. Here, we coalesce the most common challenges found in large
95 ensembles into one reference paper and discuss not only the solutions and potential alternatives, but also
96 the purposes and interpretability of these methods. EOFs are powerful tools, however their limitations
97 need to be acknowledged when applied to climate data.

98

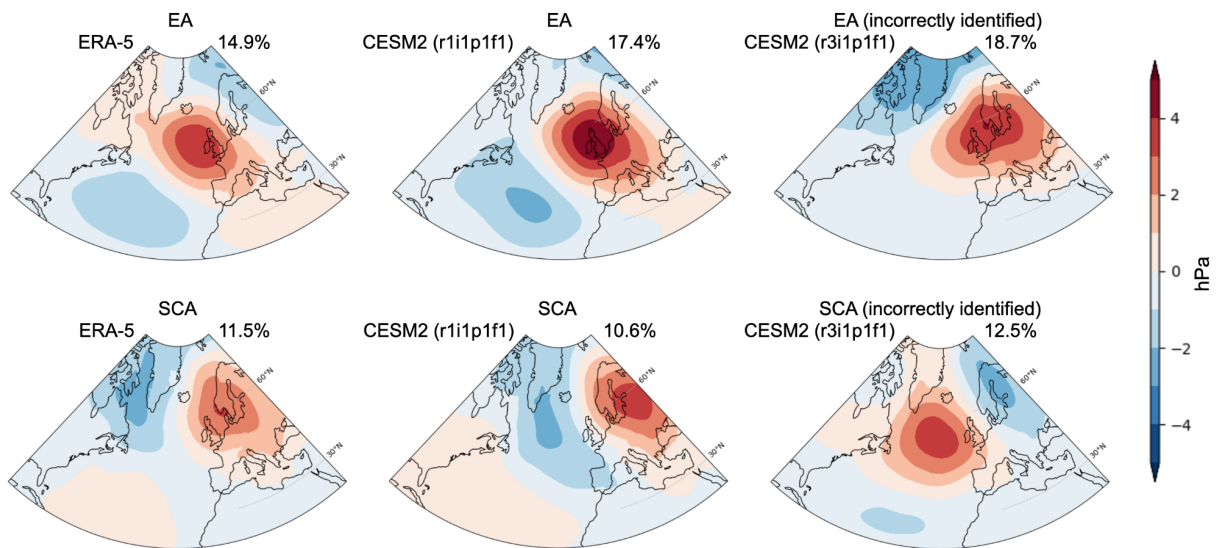
99 **Challenges with EOFs**

100 *Mode swap*

101 Sequential EOFs for a given variable are ranked by the percentage of variance they explain. When two
 102 modes explain very similar amounts of variance, mode swapping can occur, i.e, a physical mode gets
 103 paired with a neighboring EOF rather than its canonical pattern. We define mode swapping as the
 104 misassignment of a mode of variability to an adjacent EOF. Mode swapping shows up whenever EOFs
 105 are not clearly distinguishable, for example by the North's test for Rule of Thumb for EOF significance³
 106 which evaluates separability by estimating the sampling uncertainty in the associated eigenvalues.

107

108 To illustrate with a large ensemble framework, consider wintertime, January-March (JFM) sea level
 109 pressure over the North Atlantic Region (20:80°N, -90:40°E). In the ERA-5 reanalysis, EOF2 (East
 110 Atlantic Pattern, EA) accounts for 14.9% of variance and EOF3 (Scandinavian pattern, SCA) for 11.5%,
 111 only a 3.4% difference. If another dataset, or model shifts the gap by $\geq 3.4\%$, EOF2 and EOF3 swap: the
 112 second EOF now looks SCA-like and the third EA-like. A similar swap can also happen between EOF3
 113 and EOF4, pushing SCA into EOF4. Figure 1 shows this in two CESM2 (Community Earth System
 114 Model version 2) CMIP6 ensemble members. In r1i1p1f1, EOF2 matches the EA pattern with the larger
 115 variance (upper middle compared to upper left panels). In r3i1p1f1, the larger variance aligns with SCA
 116 rather than EA (compare upper right with lower left).



117

118 **Figure 1:** East Atlantic pattern (EA, row 1) and Scandinavian pattern (SCA, row 2) shown for ERA5
119 (first column), CESM2 ScenarioMIP ensemble member r1i1p1f1 (second column) and CESM2
120 ScenarioMIP ensemble member r3i1p1f1 (third column). Mode swapping is evident in the third column.
121 EA and SCA are defined as the 2nd and 3rd EOF patterns of area-weighted PSL computed over 20:80°N,
122 -90:40°E for JFM 1979-2022. Units are in hPa and variance explained is listed at the top right of each
123 panel.

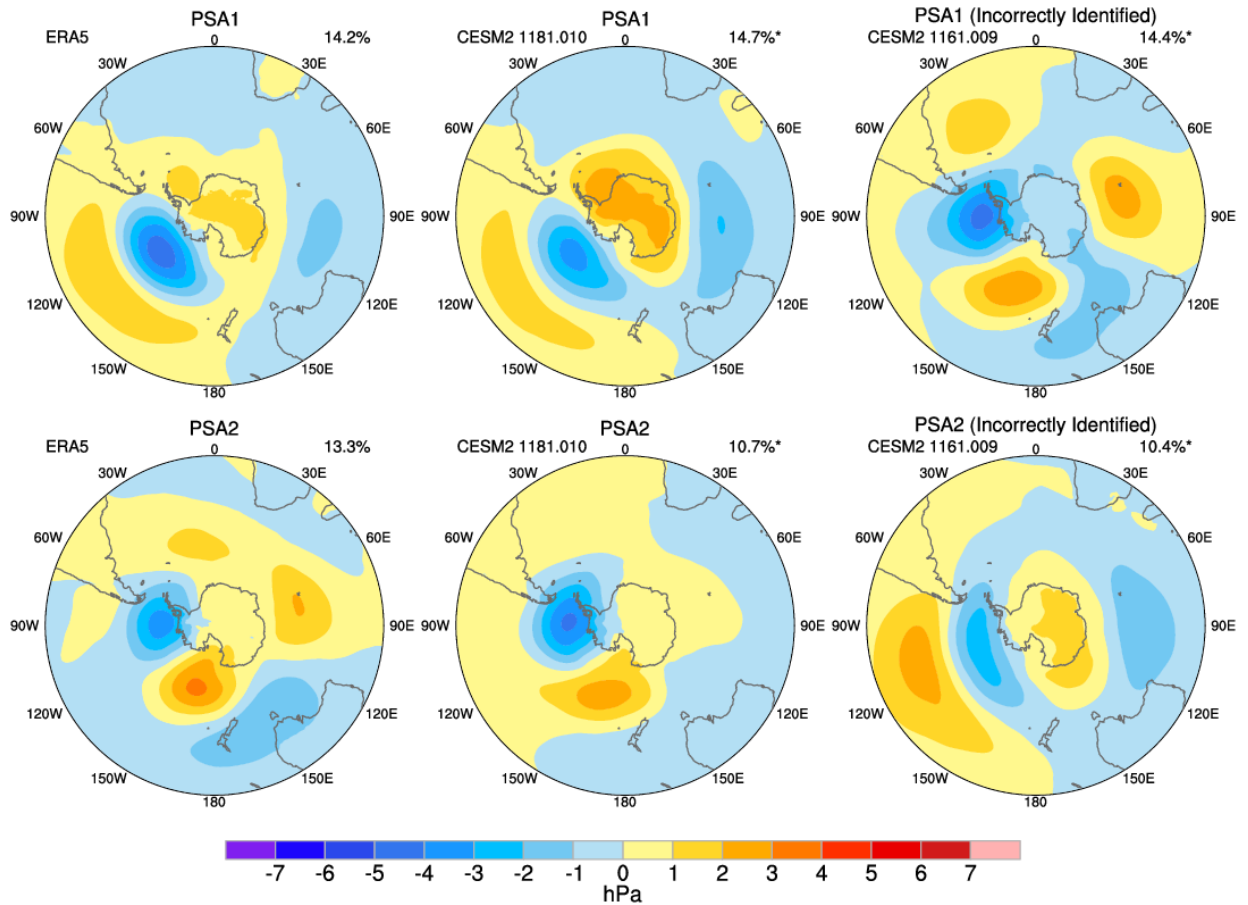
124
125 The same phenomenon occurs in the Southern Hemisphere with the Pacific South American patterns
126 (PSA1 and PSA2, Figure 2). Using sea level pressure for the winter months of June through August (JJA)
127 in the southern hemisphere, ERA5 reanalysis quantifies these modes as even more closely varying with a
128 mode separation of only 1%. Not surprisingly, when using ensemble climate model data, mode swapping
129 occurs frequently across ensemble members. As in Figure 1, the middle panels of Figure 2 show a CESM
130 ensemble member (1181.010) for which modes match the expected patterns compared to ERA5, and the
131 PSA1 and PSA2 correspond to EOF2 and EOF3, respectively. The panels on the right show a different
132 ensemble member (1161.009) where the modes have been swapped. Here PSA1 corresponds to EOF3,
133 and PSA2 to EOF2. Mode swapping amongst different realizations of the same model can have serious
134 implications when diagnosing teleconnections and their respective regional weather impacts. To
135 demonstrate potential erroneous impacts and illustrate the ubiquitousness of mode swapping in
136 ensembles, we provide an example of mode swapping frequency between PSA1 and PSA2 in Table1
137 using the CMP6 archive, with and without the removal of the forced response (defined as the removal of
138 the ensemble mean). Percentage metrics are highly dependent on sampling. For example, if the full
139 CESM and E3SM large ensembles are used, instead of the CMIP6 archive subset, the percentage statistics
140 change such that E3SM1,2 mode swaps with the forced response occur 88% and 86% of the time
141 respectively, and CESM1,2 18% and 56%. With the forced response removed these metrics are 53%,
142 48%, 33%, 44% respectively.

143

144

145

146



147

148 **Figure 2:** Pacific South American (PSA) modes 1 (row 1) and 2 (row 2) shown for ERA5 (first column),

149 CESM2 Large Ensemble member 1181.010 (second column) and CESM2 Large Ensemble member

150 1161.009 (third column). Mode swapping is evident in the third column. PSA1 and PSA2 are defined as

151 the 2nd and 3rd EOF patterns of area-weighted PSL computed over 20:90°S, 0:360°E for June-August

152 1950-2023. Units are in hPa and variance explained is listed at the top right of each panel. The patterns

153 are created by regressing global PSL anomalies onto normalized PC timeseries.

Mode Swap (%)		
MODEL/CASE	wFR (PSA1/2)	rmFR (PSA1/2)
E3SMv1	93	43
E3SMv2	90	48
CESM1	15	32
CESM2	54	41
ACCESS-ESM1-5	70	40
CanESM2	58	28
CanESM5	28	8
CSIRO-Mk360	53	3
EC-Earth3	62	50
GFDL-CM3	40	10
GFDL-ESM2M_v2	87	60
GFDL-SPEAR	73	40
IPSL-CM6A	67	67
MIROC6	2	6
MIROC-ES2L	0	0
MPI-GE-CMIP6	60	27
MPI-GE	61	26

154

155

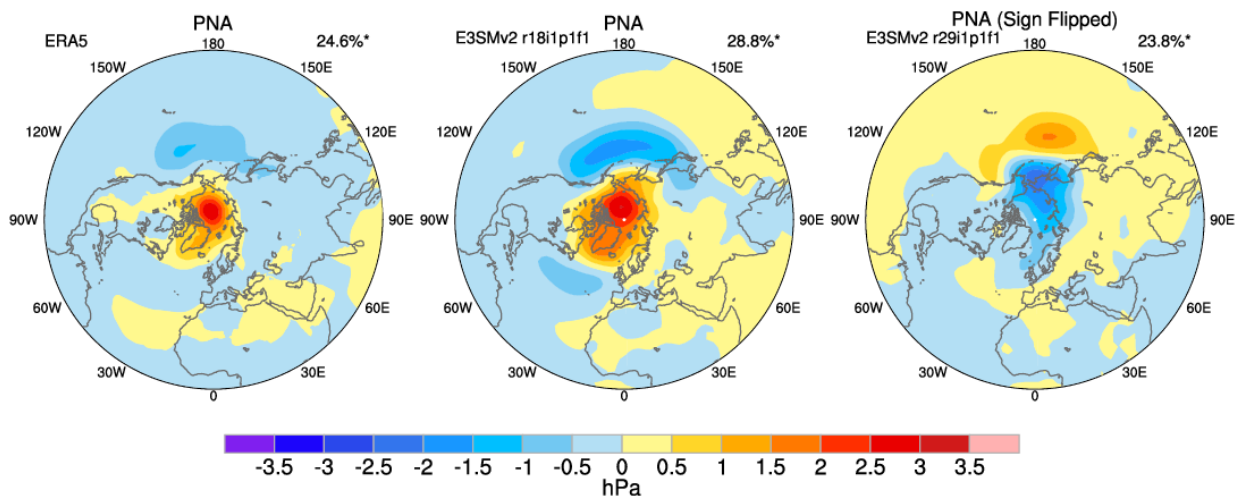
156 Table 1. Percentage of time mode swapping occurs between PSA1 and PSA2 for JJA (Southern
 157 Hemisphere winter) for the period of 1950-2022 using the CMIP6 archive. The left column names the
 158 model, the middle column shows statistics with the forces response included (wFR) and the right column
 159 shows statistics with the forced response removed (rmFR). The forced response is computed as the
 160 ensemble mean sea level pressure (SLP), which is removed from the SLP field prior to calculation of the
 161 PSA1 and 2 modes for each fully coupled ensemble. More detail in Methods. Note percentage metrics are
 162 highly dependent on method of sampling and should not be used as exact characteristics of modelling
 163 frameworks, rather as a demonstration of the depth of the mode swapping challenge for researchers.

164 *Sign flip*

165 Sign flipping is another common feature and can occur with almost any mode of variability. In EOF
 166 analysis, the sign of each EOF mode is arbitrary, due to the symmetric characteristics of eigenvalue
 167 decomposition. Flipping the sign of both the spatial pattern and its PC time series does not impact their
 168 interpretation or statistical significance. However, when comparing across models or simulations,
 169 inconsistencies in sign conventions may cause visual discrepancies and introduce challenges in statistical

170 comparison, thus we include it here. To illustrate this point, we plot the Pacific North American (PNA)
 171 pattern (Figure 3) using the Energy Exoscale Earth System Model version 2 (E3SMv2) large ensemble as
 172 defined by the first EOF pattern of area-weighted PSL computed over 20°:85°N, 120°E:120°W for June-
 173 August 1950-2022. The hemispheric pattern is created by regressing global PSL anomalies onto the
 174 normalized PC timeseries. Knowing the correct phasing (positive or negative) for the mode based on
 175 observations allows us to identify and correct sign flipping issues.

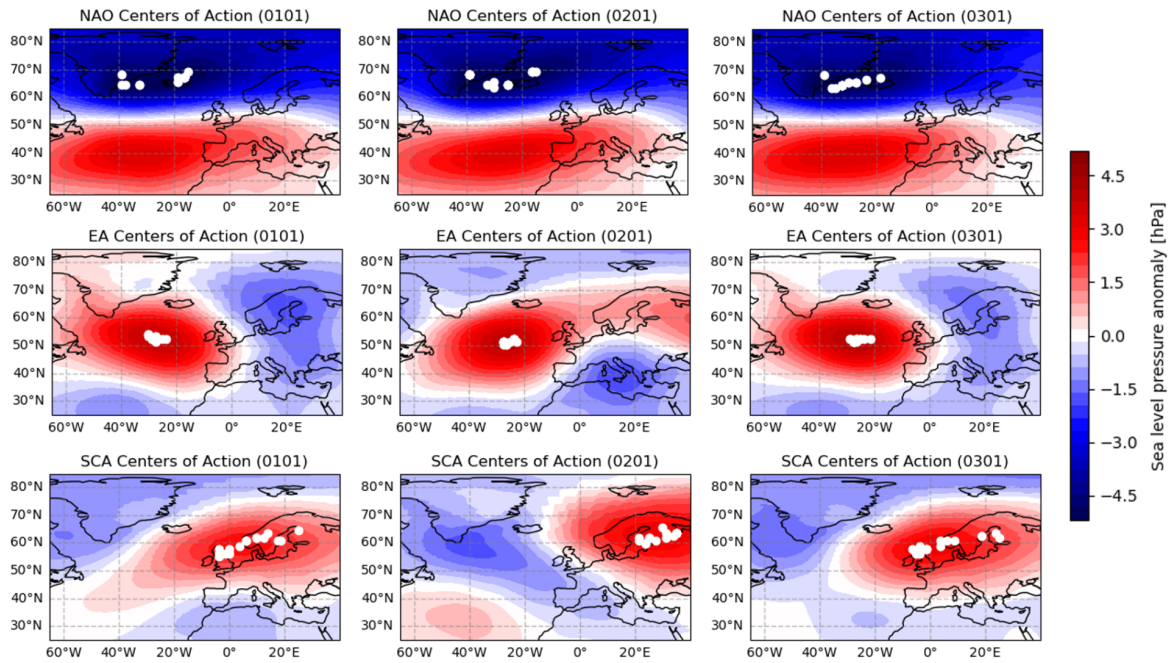
176



177

178 **Figure 3:** Pacific North American pattern shown for ERA5 (first panel), E3SMv2 member r18i1p1f1
 179 (second panel) and E3SMv2 member r29i1p1f1 (third panel). Sign flipping is evident in the third panel.
 180 Units are in hPa and variance explained for each pattern is listed at the top right. The PNA is defined as
 181 the first EOF pattern of area-weighted PSL computed over 20°:85°N, 120°E:120°W for June-August 1950-
 182 2022. Units are in hPa and variance explained is listed at the top right of each panel. The patterns are
 183 created by regressing global PSL anomalies onto normalized PC timeseries.

184

185 *Center of action variability*

186

187 **Figure 4:** Center of action variability for North Atlantic Oscillation (top), East Atlantic (middle) and
 188 Scandinavian (top) patterns computed for three ensemble members of the E3SMv2 Large Ensemble: 0101
 189 (left), 0201 (center), and 0301 (right), for a combination of historical and SSP370 simulations. The NAO
 190 is defined as the first EOF, the East Atlantic pattern as the second EOF and the Scandinavian pattern as
 191 the third EOF of area-weighted PSL computed over 20:80°N, 90°W:40°E for January-March over 100-
 192 year periods staggered by 10 years. The mean EOFs are shown, as well as the centers of action for each of
 193 the sixteen 100-year periods between 1850 and 2100, marked by white dots.

194

195 While center-of-action variability is not a flaw of PCA, it does highlight an important limitation of fixed-
 196 pattern decompositions: PCA assumes temporally invariant spatial structures. Shifts in the location of the
 197 center-of-action, defined as the geographic location of the maxima and minima associated with an EOF
 198 pattern, do occur, and can be used to evaluate multi-model, ensemble, or temporal variability. We use
 199 temporal variability to illustrate the concept. EOFs are typically calculated from a single time interval,
 200 implicitly treating mode structure as temporally invariant. However, this is not always the case, especially

201 when EOFs are applied to data generated in a changing climate. While data can be detrended prior to
202 computation of the EOFs, this is typically done by fitting simple trends and can miss more complex
203 climate change signals. When climate modes exhibit shifts in their centers of action, these shifts may be
204 represented as amplitude changes or rotations among neighboring EOFs, complicating interpretation.
205

206 To investigate temporal center-of-action stability, we calculated EOFs from successive 100-year segments
207 of simulations spanning historical and SSP370 scenarios from 1850 to 2100 for three members of the
208 E3SMv2 Large Ensemble (0101, 0201, and 0301). The start date of each 100-year segment is advanced
209 by ten years between windows, resulting in sixteen time slices for each ensemble member. Figure 4 shows
210 the centers of action for the leading three EOFs of PSL, corresponding to the North Atlantic Oscillation
211 (NAO), EA, and SCA, respectively. The loading patterns are averaged over the sixteen time slices and
212 shown as contours in the background. Centers of action are marked as white dots. If EOF patterns showed
213 no temporal variability, all white dots would cluster tightly over the maximum of the average loading
214 pattern. However, we see that they trace out a broad region of variability, especially for the NAO and
215 SCA patterns (Figure 4). This scatter demonstrates that even the leading modes of variability exhibit
216 significant non-stationarity over multi-century timescales. To quantify whether two spatial patterns can be
217 considered the “same” climate mode in the presence of sampling uncertainty - a spatial analog to the
218 North (1982)³ eigenvalue criterion - we computed the pairwise pattern-correlation distribution across all
219 time-slices. For a perfectly stable mode, correlations would cluster tightly near 1. While this holds for the
220 NAO, with 88%, 88%, and 100% of r values above 0.8 for ensemble members 0101, 0201, and 0301,
221 respectively, we find a wide, often near-uniform spread from 0 to 1 for EA and SCA. (EA: 58%, 96%,
222 and 53%, SCA: 44%, 34%, and 30%). These results indicate that higher-order EOFs exhibit far lower
223 robustness, consistent with rotational degeneracy and sensitivity to non-stationary forcing. Overall, this
224 demonstrates that spatial shifts in mode structure constitute a significant, and often underappreciated
225 source of uncertainty. When EOFs derived from historical or control simulations are projected onto future

226 climate scenarios—especially under strong anthropogenic forcing—these shifts are likely to accelerate,
227 potentially biasing our interpretation of circulation changes and feedbacks.

228

229 **Direct adjustment methods**

230 *Mode swap*

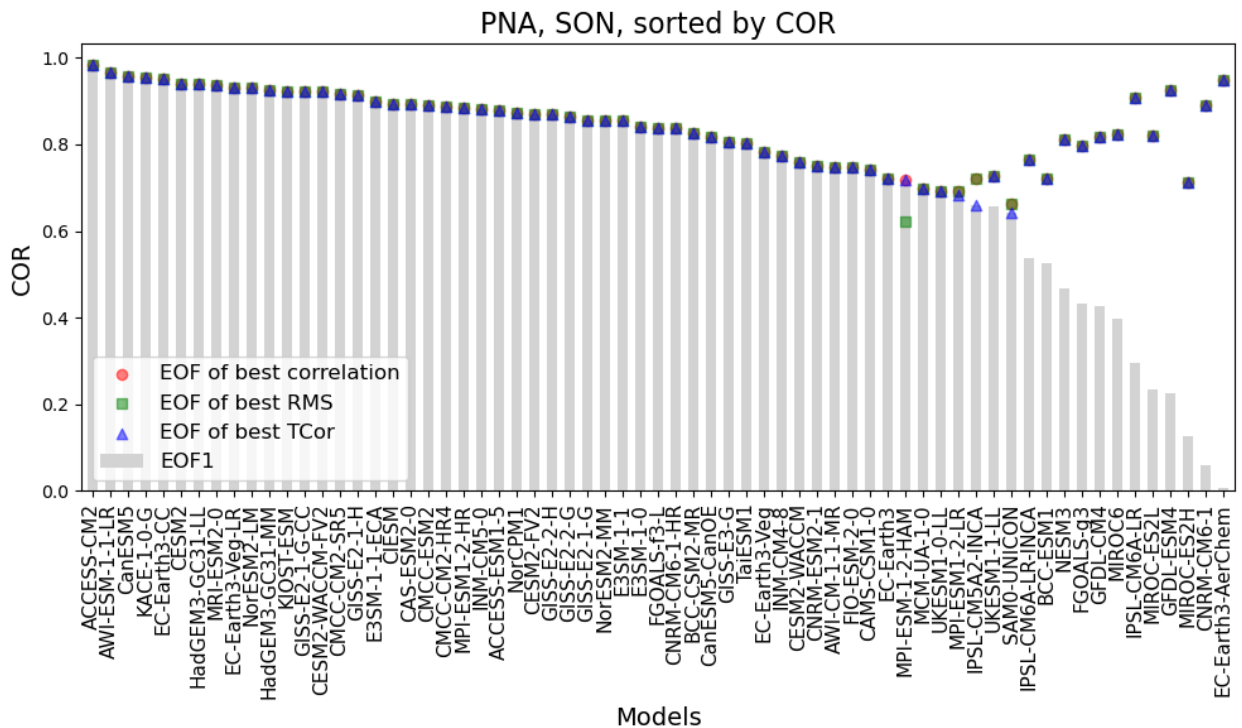
231 Mode swapping complicates both the physical interpretation and statistical comparison of EOFs, and
232 addressing it is essential for studies of climate variability given physical patterns and data structures are
233 used in tandem. Often, researchers resort to manual mode swapping to ensure consistency in mode
234 identification. While this approach can be effective for small datasets, it is tedious, subjective, and
235 impractical for large ensembles or multi-model comparisons.

236

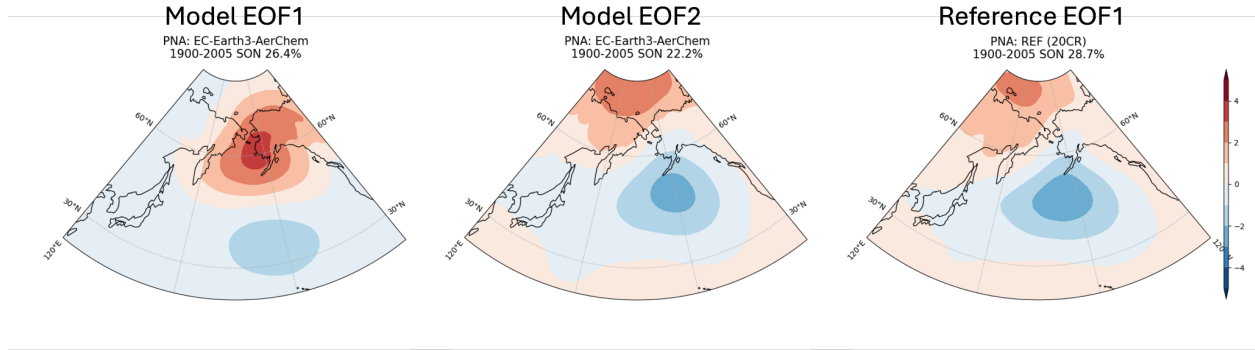
237 Recent efforts have focused on automating the mode-swapping process, using objective criteria to match
238 modes across datasets. One such technique involves statistical matching, where EOF modes from a target
239 dataset (i.e., a model simulation) are compared to those from a reference dataset using similarity metrics
240 such as spatial correlation, root-mean-square error (RMSE), or temporal correlation of the EOF PC time
241 series to the Common Basis Functions (CBF)⁸ (Table 2 and Methods) derived PC time series. Methods
242 such as CBFs have been developed to address some of the limitations of traditional EOFs. Such similarity
243 metrics allow the user to quantify the differences between the mode in question and a reference control.
244 For example, each EOF mode from the target dataset (e.g., EOF 1, EOF 2, EOF 3) is compared against a
245 specific reference mode (e.g., REF EOF 1), and the mode with the highest correlation or lowest RMSE is
246 selected as the best match. We considered the first three EOF modes after conducting the North Test³
247 to examine robustness of each order of EOF modes, where we observed a significant decrease of the
248 percentage of explained variability for EOF modes higher than the third in most cases. In some cases, the
249 reference PC time series used for temporal correlation may be derived from the CBF, particularly when
250 day-to-day or year-to-year reproducibility is not expected—for instance, in simulations following the

251 Historical or AMIP experiment protocols of CMIP. While this approach can automatically resolve most
 252 cases of EOF mode swapping (see Fig. 5, upper panel), it is not always applicable in a consistent way
 253 —particularly when different similarity metrics identify different best-matching modes. Figure 5 (bottom
 254 panel) illustrates this for the PNA pattern during SON, which is one of the modes and seasons with the
 255 highest incidence of EOF swapping ⁸. A few models display non-overlapping markers, indicating
 256 disagreement in mode identification and necessitating manual inspection and mode swapping.
 257 CBF approaches emphasize dynamical consistency and interpretability, reducing ambiguity in mode
 258 identification by using dominant modes from reference datasets as fixed bases to detect similar patterns in
 259 model output—thereby eliminating the need for post-hoc mode swapping.

260
 261
 262
 263
 264
 265



266



267
268

269 **Figure 5.** Mode swapping pattern correlation adjustment method illustration. (Upper panel) Pattern
 270 correlation of CMIP6 models' Pacific/North American (PNA) pattern during the September-October-
 271 November (SON) season (upper panel). The PNA pattern for each model was determined by the leading
 272 Empirical Orthogonal Function (EOF 1) of sea level pressure fields. Pattern correlation was then
 273 calculated between each model's EOF 1 spatial pattern and the 20th Century Reanalysis (20CR) PNA
 274 pattern (SON season). For each model, the pattern correlation of the leading three EOFs (EOF 1-3) was
 275 assessed against the 20CR PNA using spatial pattern correlation, Root Mean Square Error (RMSE), and
 276 temporal correlation between the EOF principal component (PC) time series and a Common Basis
 277 Function PC time series. The highest pattern correlation achieved after potentially swapping EOF modes
 278 based on these criteria is indicated by markers, while the pattern correlation of the original EOF 1 is
 279 shown as a gray bar. The increasing spread between EOF1 and the alternative EOF on the right
 280 demonstrates the difficulty in automated selection of the best-matching EOF mode for models on the
 281 right, which highlights challenges in systematically identifying robust climate patterns across different
 282 models (further details in Lee et al., 2019⁸). (Lower panel) Spatial pattern of model's EOF 1 (left), 2
 283 (middle) and reference dataset's EOF 1 demonstrating an example EOF swap case, obtained from EC-
 284 Earth3-AerChem model (far-most right in the upper panel) and the 20CR for PNA pattern during the
 285 SON season. This figure is a modified and expanded version from Figure 6 in Lee et al., 2019⁸.

286

287 *Sign Flip*

288 Evaluating the EOF sign is required to ensure consistency when evaluating or intercomparing model
289 simulations. A common manual approach involves checking the sign of each EOF spatial pattern or PC
290 time series against a reference and flipping it if necessary—again, a process that becomes impractical
291 with large datasets or ensemble analyses. To streamline this, automated sign correction techniques have
292 been applied, which typically rely on pattern correlation: the EOF from a target dataset is compared to a
293 reference pattern, and if the correlation is positive, the sign is retained; if negative, the sign is flipped.
294 This approach mirrors the strategy used in automated mode matching and provides a consistent, objective
295 way to address sign ambiguity. In addition to the correlation-based technique, region-specific sign
296 corrections provide a practical alternative and/or complementary method for ensuring EOF sign
297 consistency, particularly for specific physical modes of variability and their spatial signatures. This
298 method calculates the mean of the EOF pattern over a targeted geographical region and flips the sign if it
299 deviates from the expected convention. For example, the Pacific Decadal Oscillation (PDO) often shows
300 negative loading in the central North Pacific, while the Southern Annular Mode (SAM) is typically
301 negative over the Southern Ocean. Applying this check across predefined regions allows consistent
302 alignment with standard mode definitions and can be especially useful when correlation metrics yield
303 ambiguous results.

304
305 While both mode swapping and sign flipping aim to ensure coherent EOF representation across datasets,
306 they address distinct issues. Mode swapping corrects for *ordering ambiguities when eigenvalues are*
307 *close* or degenerate, noting that in linear algebra, degeneracy occurs when an eigenvalue (the frequency)
308 can be associated with more than one eigenvector (the mode), and also taking into consideration that
309 EOFs represent a continuum of modes and spatial patterns²⁰. Sign flipping, however, corrects for
310 *orientation ambiguities of individual modes*. Both corrections are essential for creating comparable EOF

311 structures that are physically interpretable across observations, models, ensemble members, or
312 experimental protocols.

313

314 **Alternative methods**

315 The limitations and challenges associated with EOF analysis highlighted thus far arise because PCA
316 imposes several constraints—most notably linearity, orthogonality, and an implicit assumption of
317 normally distributed fluctuations of the climate system. These limitations can limit PCA’s effectiveness
318 in capturing the full complexity of climate dynamics and feedbacks . Climate datasets frequently exhibit
319 nonlinear interactions, spatial and temporal dependencies, raising questions about these assumptions.
320 Furthermore, climate datasets often contain inherent physical constraints such as non-negativity (e.g.,
321 precipitation, concentrations, volumes). Standard EOF analysis does not enforce such constraints: its
322 linear combinations can easily reconstruct physical fields with negative values of intrinsically non-
323 negative variables. Working with anomalies does not avoid this issue. Once the climatological mean is
324 added back, the EOF reconstruction can still violate physical bounds. As a result, EOF-derived modes
325 may capture mathematically valid variability patterns while nonetheless producing physically impossible
326 states, complicating interpretation and downstream use.²¹

327

328

329 Motivated by these limitations, there is a need to explore alternative decomposition methods capable of
330 addressing more general structures inherent to climate data. This section introduces several powerful
331 approaches beyond PCA with further details in the Methods Section. We categorize these methods based
332 on a few criteria and provide examples applied to climate questions:

- 333 • **EOF Variants:** These techniques build off the core idea of EOFs, providing slight tweaks to try
334 and overcome one or more limitations. Examples include common basis functions, rotated EOFs,
335 and sparse EOFs.

- 336 • **Linear Methods:** EOFs are a linear technique to define and discover modes, and as such, belong
 337 to a larger class of linear methods. Other examples include factor analysis (FA), independent
 338 component analysis, nonnegative matrix factorization (NMF), and Dynamic Mode
 339 Decomposition (DMD).
- 340 • **Multilinear Methods:** EOFs are discovered by flattening the spatial axis into a single dimension.
 341 Multilinear methods, such as the Canonical Polyadic Decomposition or the Tucker
 342 Decomposition generalize PCA to higher dimensional arrays in order to discover
 343 multidimensional modes.

344 Table 2 summarizes our categorization. Each approach offers unique strengths in handling interacting
 345 relationships, temporal dynamics, and spatial topology, thus providing climate researchers with versatile
 346 tools better suited for capturing and interpreting complex patterns embedded in climate datasets. Note that
 347 this categorization is far from complete. We have chosen a small, but representative list of mode
 348 extraction methods, many of which have been applied throughout Earth system science. All the methods
 349 described here arise from linear analysis - we have chosen not to include nonlinear methods such as
 350 autoencoders²² to keep the discussion more contained. Moreover, the above methods can be combined
 351 (e.g. nonnegative Tucker Decomposition, Table 2) to add further layers of sophistication. Here, we
 352 directly compare EOFs to the methods in Table 2. In Methods, we provide an overview of the techniques
 353 and discuss which issues each method addresses.

Method	Addresses	Limitation	Category	Example Uses	Packages
EOF	Maximizes variance with orthogonal modes	Modes may mix physical signals	EOF	Gridded climate data	Many analysis software packages will have an EOF routine, but, e.g. pyEOF, CVDP, PMP.

					or DOI: 10.5334/jors.122
CBF	Shared spatial basis across datasets	May obscure dataset-specific structure	EOF Variant	Multiple models or observations in a unified spatial framework	PMP
Rotated EOF	Localized, interpretable patterns	Rotation is subjective; loses orthogonality	EOF Variant	Avoid the unphysical dipole like EOF analysis pattern	pyEOF
Sparse EOF	Enhances interpretability via sparsity	Requires tuning; sensitive to noise	EOF Variant	Fingerprinting	scikit-learn
FA	Models shared + unique variance (latent factors)	Identifiability - Different modes may explain data	Linear Method	Latent dynamics (e.g., unobserved climate drivers) are suspected to govern the observed data	scikit-learn
ICA	Finds statistically independent components	Source signals must be non-Gaussian	Linear Method	Investigate sea level pressure and water storage	scikit-learn
NMF	Nonnegative, parts-based decomposition	Non-unique; depends on initialization	Linear Method	Precipitation, cloud cover, energy fluxes; characterizing drought behavior in river basins and quantifying the sources of atmospheric particles	scikit-learn
DMD	Extracts coherent	Assumes linear	Linear Method	Traveling waves, oscillations, and	pydmd

	dynamical modes	dynamics; sensitive to noise		instabilities in geophysical flows and climate systems; LIMs	
CP Decomposition	Multivariate generalization of EOF	Non-orthogonal; difficult optimization and scaling	Multilinear Method	Application that preserves multidimensional information (e.g. e.g., spatial modes, temporal modes, ensemble modes)	tensorly
Tucker Decomposition	Multi-mode compression with core interactions	Interpretation can be nuanced; requires mixing tensor	Multilinear Method	Application that preserves multidimensional information (e.g., e.g., spatial modes, temporal modes, ensemble modes)	tensorly

354 Table 2. Summary of fixing or alternate techniques for EOF issues, including available software
355 packages addressing issues, limitations, and example uses. References and detailed descriptions of
356 specific methods and terms are found in the Methods section.

357

358 **Alternative Method Comparisons**

359 We now compare and contrast a sample of each method category (EOF variant, linear, multilinear) with
360 EOF analysis. Examples for other methods can be found in the Appendix. The aim of this section is not
361 to extract deep insights about the Earth system, but to illustrate how these tools can be applied in practice
362 and to highlight their key differences. We emphasize that our goal is to demonstrate the types of
363 additional information that can be obtained using alternative techniques. This comparison is not intended
364 to declare any single method as superior. In fact, such a direct comparison is often inappropriate, as each

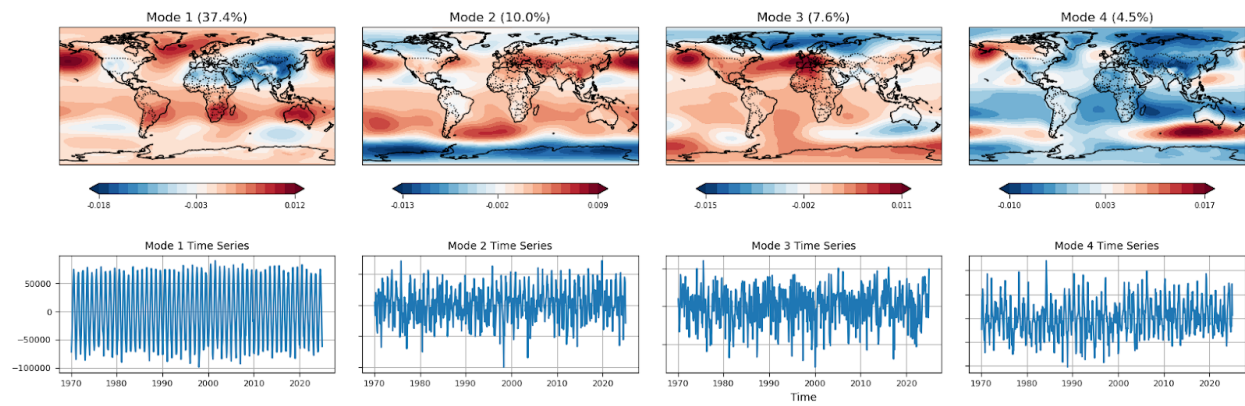
365 method is designed to capture and extract different features of the data. Each method serves a distinct
366 purpose and offers a unique perspective.

367

368 Only standard EOF analysis provides a clear and interpretable ordering of modes by importance, with
369 each mode corresponding to a descending eigenvalue and associated variance explained. The CBF
370 method (see Figure 5) inherits this property through its shared EOF basis, allowing joint variance-based
371 ranking. Rotated EOFs, however, lose this feature: although the total variance is preserved, the variance is
372 redistributed among rotated modes, and no canonical ordering remains. Sparse EOFs may allow modes to
373 be ranked by post hoc variance explained, but the presence of sparsity-inducing penalties complicates the
374 interpretation of such rankings, and ordering often depends on external criteria such as cross-validation.
375 In FA, modes can sometimes be heuristically ranked using loadings or commonalities; however, this
376 ranking is neither unique nor necessarily stable across model specifications. ICA offers no natural mode
377 ordering, as its objective is statistical independence rather than variance maximization. Similarly, NMF
378 yields additive components without orthogonality or ordering, and the contribution of each mode must be
379 assessed in context. DMD modes can be ordered by growth or decay rate, oscillation frequency, or modal
380 energy, depending on the application. CPD lacks a natural ordering entirely, as components are not
381 orthogonal and no scalar criterion governs their contribution. Tucker decomposition offers a partial
382 analogue of variance-based ordering within each mode through the singular values of the factor matrices,
383 but the presence of a dense core tensor, which mixes contributions across modes, precludes a globally
384 interpretable ranking of importance. Because most alternatives lack a coherent mode ordering, spatial and
385 temporal structures are not directly comparable. Nonetheless, we highlight representative modes from a
386 sample from each category (EOF variant, linear method, multilinear method, Table 2) based on the
387 considerations outlined above. Examples for methods in Table 2 not shown in the main text, are in the
388 Appendix, for reference.

389

390 For our baseline, we compare against the sea level pressure (PSL) EOF modes from a single run of the
 391 CESM2 large ensemble monthly historical output. For this EOF baseline, even though it is standard
 392 practice to remove the seasonal cycle before computing EOFs because it often dominates the variance, we
 393 have chosen to not remove the seasonal cycle, nor apply any type of temporal filtering which can
 394 drastically change EOF results. We have made this decision for illustrative purposes so that we have a
 395 consistent baseline against other methods. Note that removing the seasonal cycle helps focus the EOF
 396 decomposition on interannual and longer-term variability rather than the predictable annual oscillation.
 397 Examples of differences due to temporal filtering can be found in the Methods section under *Techniques:*
 398 *Standard EOF Computation*. Figure 6 contains the top four EOF modes sorted by explained variance.
 399



400
 401 Figure 6. PSL EOFs 1,2,3,4 (with percent variance explained) and respective PC timeseries for CESM2
 402 model large ensemble, first member. No temporal filtering is done for consistency and comparison across
 403 alternative methods. See the Methods section under *EOF: Standard Computation* for an illustration on the
 404 potentially large differences due to temporal filtering.

405

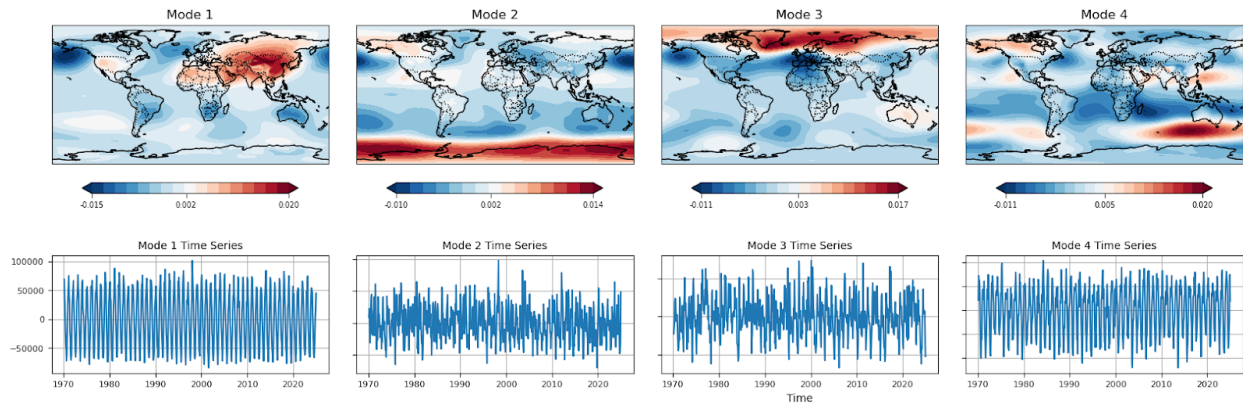
406 *Rotated EOFs (EOF Variant)*

407 The rotated EOFs produce results that are broadly similar to those from standard EOF analysis (Figure 7).

408 The first three modes largely mirror the original EOFs, aside from sign changes and minor variations in

409 spatial structure. The most notable deviation occurs in the fourth mode, where the spatial pattern differs
 410 indicating that rotation has reoriented the variance into a distinct structure not present in the unrotated
 411 EOFs.

412



413

414 Figure 7. As in Figure 6, but an example of rotated EOF.

415

416 *Factor Analysis (Linear Method)*

417 FA results begin to diverge more noticeably from those of standard EOFs (Figure 8). A mode closely

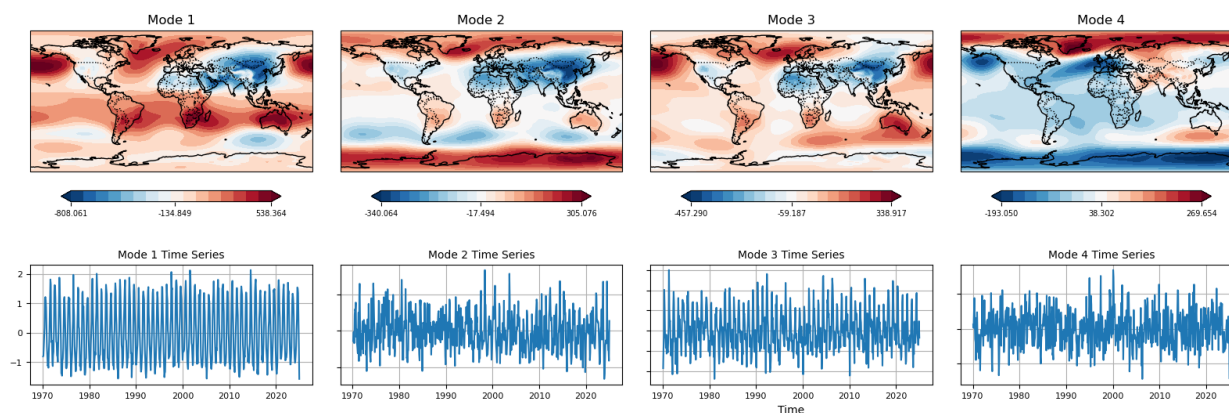
418 resembling the leading EOF still emerges, but subsequent FA modes appear as mixtures of multiple EOF

419 patterns. For example, FA mode 2 resembles a combination of EOFs 1 through 3, while FA mode 3 aligns

420 primarily with EOF 1 but includes features of EOF 4. FA mode 4 appears to blend characteristics of EOFs

421 2 and 3.

422



423

424 Figure 8. As in Figure 6 but using Factor Analysis.

425

426 *Tucker Decomposition (Multilinear Method)*

427 The Tucker decomposition is a multivariate generalization of the singular value decomposition (SVD)

428 that extracts separate sets of modes for latitude, longitude, depth, etc. In practice, it works by finding a

429 dominant subspace just like SVD but for each dimension individually which gives modes. Tucker also

430 discovers the linear mixing of these modes in a small “core” tensor. These modes can be weighted and

431 combined to reconstruct the full spatiotemporal field. Tucker allows independent control over the number

432 of modes (ranks) in each dimension. For example, with a multirank of (5, 10, 10) - i.e., 5 temporal, 10

433 latitude, and 10 longitude modes - the core tensor has 5 temporal slices, each describing how to combine

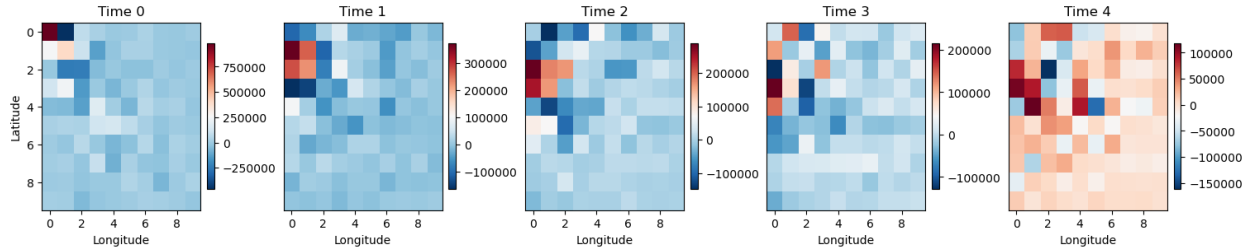
434 the 10 latitude and 10 longitude modes to form spatial patterns associated with a given temporal mode

435 (Figure 9).

436

437

438

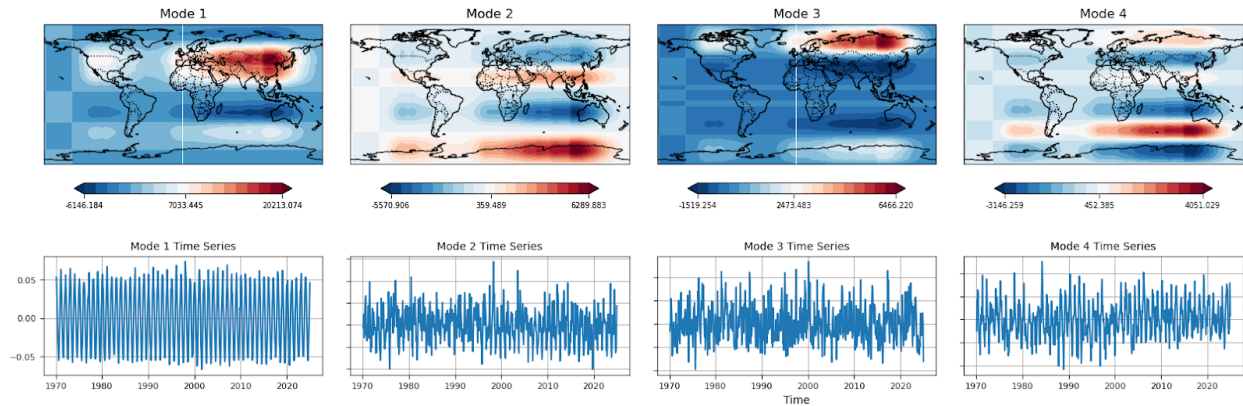


439

440 Figure 9. Tucker decomposition core tensor of PSL CESM2 large ensemble member in Figure 6, with a
 441 multirank of (5, 10, 10), with temporal modes 0 through 4, 10 latitudes (y-axis) and 10 longitudes (x-
 442 axis).

443

444 By identifying the largest weights in the core tensor, we can isolate the most dominant spatial structures
 445 associated with each temporal mode. Using this approach, we construct the leading spatial modes for the
 446 first four temporal components (Figure 10).



447

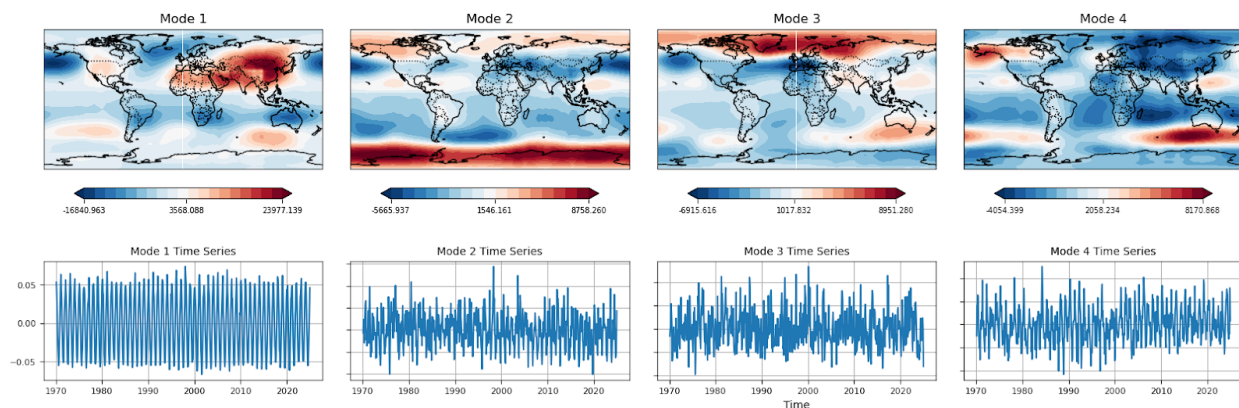
448 Figure 10. As in Figure 6, but for Tucker decomposition for the first four temporal components using the
 449 largest weights.

450

451 Importantly, the core tensor enables flexible linear combinations of spatial and temporal modes, offering
 452 richer analysis. This reconstruction is obtained by contracting the core tensor with the factor matrices,
 453 equivalently summing over rank indices the weighted outer products of the corresponding mode vectors,
 454 with the contraction weights given by the entries of the core tensor. This multilinear contraction preserves
 455 interactions across modes and reduces to standard matrix multiplication in the two-way (SVD) case.

456 When all core weights are used in combination (Figure 11), the reconstruction recovers the baseline EOF
 457 structure (up to potential sign differences), demonstrating that Tucker generalizes EOFs while retaining
 458 interpretability through its separable and multi-ranked structure.

459



460

461 Figure 11. As in Figure 9, except using all core weights in combination.

462

463 The primary benefit of the Tucker decomposition is that it does not need to flatten data fields into vectors
 464 to perform its analysis. As such, the Tucker decomposition is naturally suited for multi-way analysis
 465 where coupled structure and interactions are difficult to ascertain through vectorization. Examples
 466 include evolution of 3D variables such as ocean and atmosphere, cross-multivariable interactions, or
 467 multi-model ensemble outputs. Each factor matrix provides a set of dominant patterns for a single axis
 468 (e.g., space, time, variables), analogous to singular vectors of a matrix unfolding for EOFs, while the core
 469 tensor encodes how these mode-wise bases interact across dimensions. Individual Tucker components are
 470 therefore not rank-one objects. Instead, the data are reconstructed as weighted sums of outer products of
 471 mode-specific basis vectors, with the weights given by entries of the core tensor. As a result, physical or
 472 dynamical meaning does not attach to any single mode in isolation but emerges from the coupling
 473 structure in the core, which specifies which combinations of spatial, temporal, or variable patterns are
 474 active and with what strength.

475

476 **Summary and Discussion**

477 Digesting and interpreting gridded climate data is not always straightforward when computing modes of
478 variability with statistical methods. Here, using large ensembles commonly used for climate variability
479 diagnosis, we have attempted to summarize common challenges associated with the application of EOFs
480 leading to misinterpretation, and have provided some examples, best practices, and alternative methods to
481 consider. It can be tempting to assign physical meaning to a statistical mode, but intention and
482 understanding of the physical processes must always come into play when evaluating the mathematics.
483 Does it make physical sense? If not, we caution readers from the overinterpretation of EOFs themselves.
484 Common challenges that manifest from EOF applications include mode swapping and sign flipping;
485 however, they are relatively easy to handle by directly operating on the EOF itself. It is our intent to
486 provide a quick reference guide (e.g., Table 2) detailing EOFs and alternative methods that broadly fit
487 into three categories: EOF variants, linear methods, and multilinear methods. Any method that extracts
488 modes of variability must be fit for purpose, always taking care to make sure modes are applicable to a
489 specific science question and avoiding misinterpretation²¹.

490

491 Not yet fully discussed, but equally important is the question of computing modes of variability under
492 climate change, now typically addressed with the application of large ensembles^{9,17}. How does one parse
493 the variability of a system when the base state, by definition, is still changing? As the Earth system
494 continues to remain out of equilibrium with the influx of anthropogenic greenhouse gas forcing, a key
495 consideration is how, and if, the forced response should be removed. There is no right answer, rather, it
496 entirely depends on the purpose and science question being asked. If one chooses to remove the forced
497 response to elucidate a baseline, natural state, then detrending the data and using anomalies to compute
498 the EOF, is a common approach. The difference between detrending, or not, can have significant
499 consequences for interpretation. In our mode swapping example in Figure 2, the difference between the
500 rate of mode swapping for PSA1 and PSA2 markedly changes depending on whether or not the forced

501 response is removed. However, even detrending and removing the forced response will not necessarily
502 remove any feedback that occurs due to the forcing itself. These types of questions inspired the creation
503 of ForceSMIP, (Forced Component Estimation Statistical Methods Intercomparison Project²³), which we
504 encourage readers to follow for a deeper dive into forced response issues^{24,8,25,26}. Finally, we
505 acknowledge that this article does not exhaustively cover all interpretation pitfalls with EOFs or statistical
506 methods, but we hope our overview, and comparison of methods, aid readers when choosing techniques
507 best suited for their science.

508

509

510 **Methods**

511 *Datasets*

512 Two reanalyses, two large ensembles, and the CMIP6 (Coupled Model Intercomparison Project Phase 6)
513 database are used to demonstrate EOF issues and alternatives. For reanalysis products, we sample sea
514 level pressure (PSL) at monthly intervals for the period of 1950-2023, from the ECMWF reanalysis,
515 version 5, (ERA5)²⁷, as well as the 20th Century Reanalysis (20CR)²⁸ from 1900- 2005. Both analyses
516 provide pressure level data with ERA5 regridded to 0.25° horizontal resolution and 20CR regridded to 2°
517 horizontal resolution. For large ensemble simulations suites, we utilize four sets of large ensembles from
518 fully coupled Earth system models and include: E3SMv1 and v2 (the Department of Energy's Energy
519 Exascale Earth System Model, versions 1 and 2), and CESM1 and CESM2 (the Community Earth System
520 Model, versions 1 and 2)¹⁶. Again, we analyze PSL at monthly intervals from the historical simulations,
521 where E3SMv1 employs 17 ensemble members, E3SMv2, 21 members, CESM1 (40 members), and
522 CESM2 (50 members). E3SM employs the E3SM Atmosphere model (EAM) and the Model for
523 Prediction Across Scales-Ocean: MPAS-Ocean, whereas CESM employs the Community Atmosphere
524 model (CAM) and the Parallel Ocean Program, version 2 (POP2). Further details on versions 1 and 2 for
525 both modelling frameworks are found in the respective modelling documentation papers^{29,30,31,32}. From the

526 CMIP6 archive, we utilize PSL at monthly intervals for the historical simulations for the same period as
527 the 20CR. In addition to E3SM and CESM, CMIP6 archive models^{8,9} included in Table 1 include
528 ACCESS-ESM1-5, CanESM2, CanESM5, CSIRO-Mk360, EC-Earth3, GFDL-CM3, GFDL-ESM2M_v2,
529 GFDL-SPEAR, IPSL-CM6A, MIROC6, MIROC-ES2L, MPI-GE-CMIP6, MPI-GE.

530

531 *Techniques*

532 Here we describe all methodologies discussed including standard EOF computation, EOF alternatives,
533 and finally techniques applied to directly adjust standard EOFs. Once again here, we emphasize that there
534 is no best method for all applications. Rather, each different technique illuminates different features of
535 the data, which is helpful for different types of analysis. For every method, we will describe how it is
536 computed, and then demonstrate an application on a CESM2 LE member. The purpose is to display
537 example outputs, rather than perform any scientific analysis. Finally, for each method we will briefly
538 recap 1) the structure that the method isolates and 2) discuss when this method could be useful or limited.

539

540 *Technique: Standard EOF Computation*

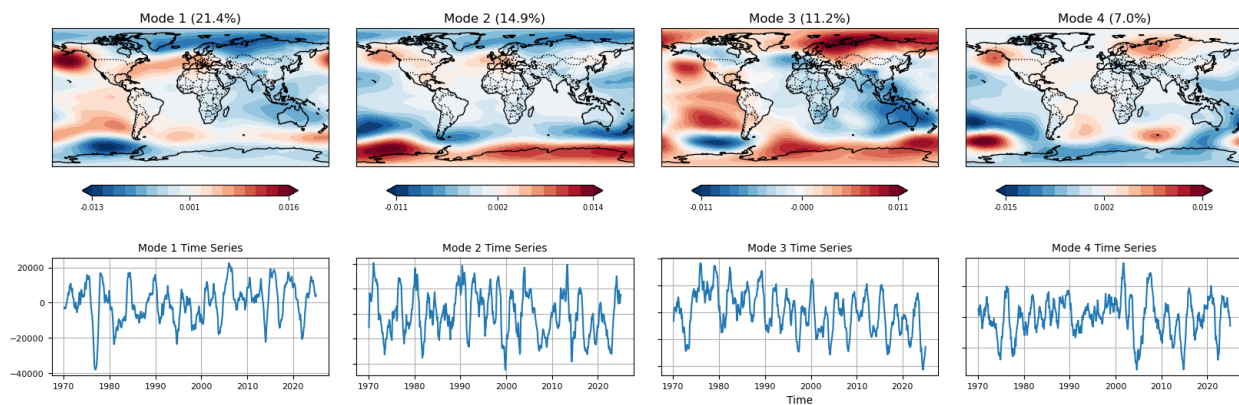
541 To allow for complete comparison between the different methods, we will briefly recap how standard
542 EOFs, or principal component analysis (PCA), is computed. Given a data matrix \mathbf{X} of dimensions $p \times n$,
543 where p is the number of spatial locations and n is the number of time steps, the data is typically centered
544 by subtracting the temporal mean at each location. The covariance matrix $\mathbf{C} = (1/n) \times \mathbf{X} \times \mathbf{X}^t$ is then
545 computed, and its eigenvalue decomposition yields orthonormal eigenvectors (the EOFs) and eigenvalues
546 that indicate the amount of variance explained by each mode. By design, the spatial patterns (the EOFs)
547 and their corresponding temporal coefficients (the PCs) are orthogonal. The **rank** of this decomposition
548 refers to the number of modes retained, i.e., how many spatial-temporal patterns are needed to
549 approximate the data well.

550

551 The explained variance is one of the strongest features of EOFs, allowing one to order the modes by
552 importance. Further, it is often the case that a few leading modes capture the majority of the total
553 variance. For this reason, EOF analysis can result in a parsimonious representation of the dynamics. The
554 orthogonality further helps to isolate uncorrelated modes. However, EOF analysis can also produce
555 patterns that are complex and challenging to interpret physically, potentially leading to misunderstanding
556 or confusion⁵. Challenges with EOF analysis include:

557

- 558 ● **Assumes data are best described by orthogonal spatial modes**, which may not correspond to
559 physically meaningful structures.
- 560 ● **Mixes physical patterns** when eigenvalues are nearly degenerate, leading to spatial modes that
561 are hard to interpret.
- 562 ● **Captures variance, not structure** — modes are ranked by explained variance, even if they do
563 not align with meaningful dynamical or physical features.
- 564 ● **Sensitive to sampling variability**, especially in the presence of noise or short time series (Figure
565 12).
- 566 ● **Assumes linear correlations** — does not capture nonlinear interactions.
- 567 ● **Applies only to two-dimensional (matrix) data** — requires flattening multidimensional arrays,
568 which discards structural information (e.g., separating space and time).
- 569 ● **Allows negative loadings**, which may be difficult to interpret in contexts like precipitation or
570 energy where signals are inherently nonnegative.
- 571 ● **Lacks uniqueness when eigenvalues are repeated**, making modes unstable across realizations
572 or datasets.



573
 574 Figure 12. As in Figure 6, except using a 1-year rolling average to demonstrate the potentially large
 575 differences when temporal filtering is applied.

576
 577 **Extracted Structure and Applicability** - Standard EOF analysis isolates orthogonal spatial modes that
 578 maximize explained variance under a linear covariance model. This makes EOFs effective at identifying
 579 the most energetic large-scale patterns and providing a compact, ordered representation of variability. The
 580 method is most useful as a baseline dimensionality-reduction and diagnostic tool, particularly for well-
 581 sampled, approximately linear systems where variance is a meaningful proxy for importance. However,
 582 because EOFs prioritize variance rather than dynamical or physical structure, they can mix distinct
 583 processes, be sensitive to sampling and preprocessing choices, and yield modes that are difficult to
 584 interpret physically. Despite these challenges, EOFs have cemented themselves as the most ubiquitous
 585 tool within Earth sciences for dimensionality reduction and mode discovery.

586
 587 Techniques: EOF Variants

588 While standard EOF analysis provides an optimal low-rank decomposition in terms of explained variance,
 589 several variants have been developed to address its limitations or to impose additional constraints
 590 motivated by scientific interpretability. These variants often modify the underlying basis functions, adjust
 591 orthogonality constraints, or introduce sparsity-promoting priors. In this section, we briefly discuss three

592 common approaches: EOF expansions using **Common Basis Functions, Rotated EOFs, and Sparse**
 593 **EOFs.**

594 *Technique - EOF Variants: Common Basis Functions*

595 The standard EOF analysis is designed for one sample matrix \mathbf{X} of data. The Common Basis Function
 596 (CBF) approach is a multivariate generalization of EOF analysis designed to extract shared spatial
 597 patterns across multiple related datasets. Naive computations of EOFs for ensembles can be derived either
 598 from computing EOFs separately for each dataset, or by stacking the data to compute combined EOFs. In
 599 contrast to stacked EOF approaches which optimize variance only in an ensemble-averaged sense and can
 600 be dominated by high-variance members, the CBF method explicitly seeks a single set of spatial basis
 601 functions that are simultaneously important across all datasets, enabling direct and consistent comparison
 602 between them.

603

604 Suppose we have M datasets $\{\mathbf{X}^1, \mathbf{X}^2, \dots, \mathbf{X}^M\}$, each of size $p \times n$, where p is the number of spatial
 605 locations and n is the number of time steps. The goal is to find a common set of orthonormal spatial basis
 606 vectors $\mathbf{B} \in \mathbb{R}^{p \times r}$ (i.e., $\mathbf{B}^T \mathbf{B} = \mathbf{I}$), along with dataset-specific temporal coefficients $\mathbf{S}^m \in \mathbb{R}^{r \times n}$ such that:

607
$$\mathbf{X}^m \approx \mathbf{B} \mathbf{S}^m \quad \text{for } m = 1, \dots, M.$$

608 This can be formulated as a maximum likelihood problem^{33,34}. As a result, the extracted modes
 609 exhibit a consistent ordering of explained variance within each dataset, rather than reflecting variability
 610 dominated by a subset of ensemble members. The CBF method is particularly useful when comparing
 611 multiple models or observations in a unified spatial framework^{39,35}.

612 **Extracted Structure and Applicability** - The CBF approach isolates a shared set of orthonormal spatial
 613 modes that jointly maximize explained variance across multiple related datasets. This makes explicit the
 614 spatial structures that are common to all datasets while allowing their temporal evolution to differ,

615 enabling direct cross-dataset comparison in a unified basis. CBF is particularly useful when analyzing
 616 ensembles, multi-model archives, or observational–model comparisons where structural alignment is
 617 desired. However, because the method still prioritizes variance and enforces a single global spatial basis,
 618 it can suppress dataset-specific features and remains subject to the same linearity and interpretability
 619 limitations as standard EOF analysis.

620 Technique - EOF Variants: Rotated EOFs

621 While standard EOFs are optimal in terms of explained variance and form an orthogonal basis, their
 622 spatial patterns often suffer from poor, unphysical interpretability, especially when modes have nearly
 623 equal eigenvalues and represent mixtures of physical structures. **Rotated EOFs (REOFs)** attempt to
 624 address this by applying a rotation—typically orthogonal or oblique—to a subset of the leading EOFs to
 625 produce more localized and physically interpretable patterns^{36,37}. Compared to standard EOFs, REOFs
 626 trade orthogonality and variance ordering for better physical localization and interpretability, especially in
 627 the presence of degeneracies among leading modes⁹.

628 The procedure begins with standard EOF analysis to obtain the leading r EOF loading vectors, typically
 629 denoted $\mathbf{L} \in \mathbb{R}^{p \times r}$, where p is the number of spatial points. An orthogonal matrix $\mathbf{R} \in \mathbb{R}^{r \times r}$ ($\mathbf{R}^T \mathbf{R} =$
 630 $\mathbf{R} \mathbf{R}^T = \mathbf{I}$) is then applied to yield new, ‘rotated’ loadings:

$$631 \quad \mathbf{L}' = \mathbf{L} \cdot \mathbf{R},$$

632 where \mathbf{R} is chosen to optimize some criterion. Probably the most common method is the **Varimax**
 633 objective, which maximizes the variance of squared loadings across modes³⁸. The corresponding
 634 rotated principal components (temporal coefficients) are $\mathbf{S}' = \mathbf{R}^T \cdot \mathbf{S}$, where \mathbf{S} contains the original
 635 principal components. This transformation preserves the total variance and subspace spanned by the
 636 original EOFs, but the rotated modes are no longer orthogonal. REOFs yield regionalized patterns that
 637 depend on the number of retained modes. When only a few modes are used, the patterns can be highly

638 sensitive to changes in r . As r approaches the number of spatial grid points, ROEFs tend to localize into
639 patterns centered around individual points.

640 Previous studies have shown that REOF analysis is able to avoid the unphysical dipole-like EOF analysis
641 pattern that often appears when the known dominant mode has the same sign across the domain and to
642 simplify spatial structures while retaining the robust patterns^{21,39}.

643 **Extracted Structure and Applicability** - Rotated EOF analysis isolates spatial modes within the leading
644 EOF subspace that are optimized for localization and interpretability rather than variance optimality. This
645 rotation makes physically coherent and regionally confined patterns more explicit, particularly when
646 standard EOFs mix structures due to near-degenerate eigenvalues. REOFs are most useful when
647 interpretability of spatial patterns is prioritized over strict orthogonality or variance ordering, such as in
648 regime or teleconnection analysis. However, the resulting modes depend on the number of retained EOFs
649 and the chosen rotation criterion, and the loss of orthogonality can complicate statistical interpretation and
650 comparison across datasets.

651 Technique - EOF Variants: Sparse EOF

652 Standard EOF analysis yields spatial patterns that are typically global in extent and difficult to interpret
653 physically when the dominant modes have broad spatial support. **Sparse EOFs** aim to improve
654 interpretability by promoting spatial localization of the modes through sparsity constraints. In this
655 formulation, spatial patterns are encouraged to have many near-zero entries, highlighting only the most
656 relevant regions contributing to variability.

657 Sparse EOFs are typically formulated as a **regularized matrix factorization** problem, where the goal is
658 to approximate the data matrix $\mathbf{X} \in \mathbb{R}^{p \times n}$ as $\mathbf{X} \approx \mathbf{B} \mathbf{S}$, with $\mathbf{B} \in \mathbb{R}^{p \times r}$ representing spatial modes and \mathbf{S}
659 $\in \mathbb{R}^{r \times n}$ the temporal coefficients, just as in standard EOFs. However, instead of requiring that the

660 columns of \mathbf{B} be orthogonal eigenvectors, the optimization adds a sparsity-inducing penalty, often the ℓ_1
 661 norm:

662 minimize $\|\mathbf{X} - \mathbf{B}\mathbf{S}\|_F^2 + \lambda \sum_k \|\mathbf{b}_k\|_1$, subject to $\|\mathbf{b}_k\|_2 = 1$ for each mode k ,

663 where \mathbf{b}_k is the k -th column of \mathbf{B} , and a penalty term $\alpha > 0$ controls the degree of sparsity⁴⁰,⁴¹. The
 664 penalty term controls the degree of sparsity - larger α results in more sparse EOFs. The result is a set of
 665 EOF-like modes that retain much of the explanatory power of standard EOFs while being easier to
 666 associate with physical mechanisms or localized features. Sparse PCA appears to have had limited
 667 application within the Earth sciences, though it has been applied for instance for more interpretable
 668 fingerprinting⁴².

669 **Extracted Structure and Applicability** - Sparse EOF analysis isolates spatial modes that explain
 670 variability while explicitly enforcing localization through sparsity constraints. This highlights regionally
 671 confined structures and suppresses weak or diffuse loadings, improving physical interpretability relative
 672 to standard EOFs. Sparse EOFs are most useful when the underlying processes are expected to be
 673 spatially localized or when interpretability of individual regions is critical, such as in detection or
 674 fingerprinting studies. However, the results depend sensitively on the choice of sparsity penalty, sacrifice
 675 strict orthogonality, and can bias variance attribution by excluding low-amplitude but dynamically
 676 relevant structures.

677 *Techniques: Linear Methods*

678 While EOFs (PCA) are among the most widely used techniques for identifying dominant patterns of
 679 variability in spatiotemporal datasets, they belong to a broader class of linear dimensionality reduction
 680 methods. Several alternative techniques—including **Factor Analysis (FA)**, **Independent Component**
 681 **Analysis (ICA)**, **Nonnegative Matrix Factorization (NMF)**, and **Dynamic Mode Decomposition**
 682 **(DMD)**—offer different decompositional frameworks based on distinct statistical or structural
 683 assumptions. These methods share the goal of representing high-dimensional data using a low-rank

684 approximation, but they differ in how the components are derived, constrained, and interpreted. In the
 685 following subsections, we compare each of these methods to EOFs, focusing on their objectives,
 686 assumptions, and implications for interpretability in the context of geophysical data.

687

688 Technique - Linear Methods: Factor Analysis

689 **Factor analysis** (FA) is a linear dimensionality reduction technique closely related to EOFs, but with a
 690 distinct modeling philosophy. While EOFs seek orthogonal directions that maximize explained variance,
 691 FA assumes that the observed variables are driven by a smaller number of **latent (unobserved) factors**,
 692 plus unique noise specific to each observed variable^{43,37}. The observed data $\mathbf{X} \in \mathbb{R}^{n \times p}$ is modeled as:

693
$$\mathbf{X} = \mathbf{F}\mathbf{\Lambda}^T + \mathbf{E},$$

694 where:

- 695 • $\mathbf{F} \in \mathbb{R}^{n \times r}$ contains the scores of r unobserved (latent) factors,
- 696
- 697 • $\mathbf{\Lambda} \in \mathbb{R}^{p \times r}$ is the loading matrix linking the latent factors to the observed variables,
- 698
- 699 • $\mathbf{E} \in \mathbb{R}^{n \times p}$ is the idiosyncratic Gaussian noise, assumed to be uncorrelated across
 700 variables and with a diagonal covariance matrix.

701

702 The assumption of FA is that the high-dimensional data arises from a low-dimensional set of underlying
 703 processes, possibly confounding or not directly observable, such as circulation regimes or hidden drivers
 704 of variability in the climate system. The noise term accounts for individual variability that is not shared
 705 between variables. Unlike EOFs, which assume all variance is shared and seek orthogonal modes, FA

706 models both shared and unique variance separately. This distinction allows FA to represent more flexible
707 and realistic relationships among variables by permitting non-orthogonal loadings, which is especially
708 useful for modeling correlated processes. While EOFs decompose the total variance in the data, FA
709 focuses specifically on capturing the covariance structure, often through maximum likelihood estimation.
710 Additionally, FA can more effectively account for measurement noise or unresolved structure, making it
711 particularly useful in settings where some factors are believed to be hidden or confounded. Factor
712 analysis is a common data analysis technique used throughout the social sciences, with limited
713 applications in the Earth sciences⁴⁴. FA is conceptually appealing in settings where latent dynamics (e.g.,
714 unobserved climate drivers) are suspected to govern the observed data.

715 **Extracted Structure and Applicability** - Factor analysis isolates latent factors that explain the shared
716 covariance among observed variables while explicitly modeling variable-specific noise. This makes it
717 well suited for identifying hidden or confounding processes that drive correlated variability, rather than
718 simply maximizing total variance. FA is most useful when measurement noise or unresolved structure is
719 believed to be substantial and when the goal is to infer underlying drivers rather than simply producing
720 orthogonal modes. However, the method relies on strong distributional and noise assumptions, does not
721 enforce spatial structure, and can be sensitive to model specification and identifiability choices.

722 Technique - Linear Methods: Independent Component Analysis

723 EOFs have as their primary objective, the successive maximization of variance of the modes. The
724 orthogonality and uncorrelatedness come as byproducts of this goal. By contrast, **Independent**
725 **Component Analysis (ICA)** has statistical independence as its main aim⁴⁵. This makes ICA especially
726 well-suited for extracting physically distinct processes when data are non-Gaussian. For Gaussian
727 variables, uncorrelatedness and independence coincide, and ICA reduces to EOF/PCA. However, many
728 climate and geophysical datasets are non-Gaussian, motivating the use of ICA as a generalization of EOFs
729 in this setting³⁷ .

730 Conceptually, ICA shares a modeling philosophy with FA: they are both latent variable models, meaning
731 that they both assume that observed variables are generated by a smaller number of latent (hidden)
732 components. The difference lies in the objective. FA explains the covariance structure of the observed
733 variables using fewer latent variables (factors). The emphasis is on modeling correlations and accounting
734 for noise. ICA seeks to find latent variables that are statistically independent and assumes that the
735 observed variables are mixtures of these independent sources. The goal is source separation. In linear
736 ICA, the model is:

737
$$\mathbf{x} = \mathbf{\Lambda} \mathbf{f},$$
 where \mathbf{f} is a vector of statistically independent components,

738 and $\mathbf{\Lambda}$ is a full-rank *mixing matrix*. The observed data vector \mathbf{x} is a linear combination of these latent
739 sources. The goal is to estimate an unmixing matrix \mathbf{W} such that:

740
$$\hat{\mathbf{s}} = \mathbf{W} \mathbf{x}$$

741 recovers the independent components $\hat{\mathbf{s}} \approx \mathbf{f}$. The optimal \mathbf{W} is obtained by minimizing a cost function
742 measuring statistical dependence, typically based on non-Gaussianity, mutual information, or entropy³⁶
743 . This objective contrasts with the variance-maximizing goal of EOFs or the likelihood-based objective of
744 factor analysis. Unlike EOFs, ICA does not impose orthogonality or rank ordering, and the decomposition
745 is not unique: the independent components are identifiable only up to permutation and scaling. ICA has
746 been used to investigate sea level pressure and water storage^{46,47}.

747 **Extracted Structure and Applicability** - Independent Component Analysis isolates latent components
748 that are statistically independent rather than merely uncorrelated or variance-optimal. This emphasizes
749 source separation and can reveal physically distinct processes in non-Gaussian data that are mixed in
750 standard EOF representations. ICA is most useful when independence is a meaningful assumption, such
751 as when multiple underlying processes contribute additively and exhibit non-Gaussian statistics.

752 However, the decomposition is not unique, lacks natural mode ordering, and can be sensitive to
753 preprocessing and noise, which complicates interpretation and comparison across datasets.

754 Technique - Linear Methods: Nonnegative Matrix Factorization

755

756 **Nonnegative Matrix Factorization (NMF)** is a linear dimensionality reduction technique that differs
757 from EOFs in one major fundamental way: it imposes **nonnegativity constraints** on both spatial and
758 temporal components. This makes NMF especially useful when the data are naturally nonnegative (e.g.,
759 precipitation, cloud cover, energy fluxes), and when interpretability is enhanced by additive, parts-based
760 representations⁴⁶. Given a nonnegative data matrix $\mathbf{X} \in \mathbb{R}^{+p \times n}$, NMF approximates \mathbf{X} as the product of two
761 low-rank nonnegative matrices:

762
$$\mathbf{X} \approx \mathbf{W} \mathbf{H},$$

763 where:

- 764
- $\mathbf{W} \in \mathbb{R}^{+p \times r}$ contains the spatial patterns (basis vectors),
- 765
- $\mathbf{H} \in \mathbb{R}^{+r \times n}$ contains the temporal activations or coefficients.
- 766

767

768 Unlike EOFs, which yield orthogonal modes with both positive and negative loadings, NMF provides
769 strictly additive components, allowing for a “parts-based” decomposition. This can yield spatial structures
770 that are localized and physically interpretable, as each field is reconstructed as a nonnegative linear
771 combination of a few basic building blocks. In contrast to EOFs, which can produce modes with large
772 canceling positive and negative values, NMF enforces nonnegativity, leading to more interpretable and
773 parts-based representations. While EOFs offer an optimal decomposition in terms of variance explained,
774 NMF prioritizes interpretability and sparsity at the cost of optimality. Unlike EOFs, NMF modes are not

775 constrained to be orthogonal or ordered by explained variance, which does bring about ambiguity of
776 importance for the underlying structures. Further, NMF lacks a unique solution and is sensitive to
777 initialization and algorithmic choices, in contrast to the closed-form solution of EOFs obtained via SVD.
778 In Earth Sciences, NMF has been applied to problems such as identifying characterizing drought behavior
779 in river basins and quantifying the sources of atmospheric particles^{49,50}.

780 **Extracted Structure and Applicability** - Nonnegative Matrix Factorization isolates additive spatial–
781 temporal components under explicit nonnegativity constraints, yielding parts-based representations of the
782 data. This highlights localized, physically interpretable structures when variables are inherently
783 nonnegative and when cancellation between positive and negative loadings is undesirable. NMF is most
784 useful for exploratory analysis and feature discovery in settings where interpretability and compositional
785 structure are prioritized over variance optimality. However, the decomposition is not unique, lacks natural
786 mode ordering, and is sensitive to initialization and algorithmic choices, which can limit robustness and
787 reproducibility.

788 Technique - Linear Methods: Dynamic Mode Decomposition

789 EOFs identify spatial patterns that capture maximal variance in the data, without directly considering how
790 those patterns evolve over time, i.e., the PCs are selected to be orthogonal. By contrast, **Dynamic Mode**
791 **Decomposition (DMD)** is a data-driven technique designed to extract spatiotemporal patterns that evolve
792 according to approximate linear dynamics. DMD is based on the idea that the temporal evolution of the
793 system can be approximated by a linear operator, which maps each snapshot of the system state to the
794 next. The resulting decomposition yields spatial patterns, each associated with a fixed temporal frequency
795 and a corresponding growth or decay rate. This makes DMD particularly well-suited for identifying
796 coherent structures such as traveling waves, oscillations, and instabilities in geophysical flows and
797 climate systems^{51,52}. There are many different algorithms that fall under the DMD category; however, in
798 its most basic form, DMD constructs the least-squares linear operator that advances snapshots forward in

799 time and directly eigendecomposes this operator to obtain modes and their associated growth or decay
800 rates⁵³. This is very similar to the Linear Inverse Modeling (LIM), and Principal Oscillation Pattern /
801 Principal Interaction Pattern (POP/PIP) methods used throughout the climate literature.

802 As clarified by Tu et al. (2013)⁵², DMD, LIM and POP/PIP methods can all be understood as estimating
803 essentially the same finite-dimensional linear evolution operator from time-lagged data, differing
804 primarily in formulation, assumptions, and historical context⁵². In LIM, this operator is estimated by
805 fitting a linear stochastic dynamical system whose deterministic component governs the mean evolution
806 of the state and whose eigenvalues characterize dominant decay and oscillatory time scales. POP/PIP
807 analysis similarly focuses on the eigenmodes of a linear propagator inferred from lag-covariance
808 statistics, with an emphasis on identifying dynamically relevant oscillatory and interacting patterns. These
809 approaches are mathematically equivalent under conditions of linear dynamics, sufficiently rich state
810 representations, evenly sampled time series, and when the same lagged least-squares estimator is used for
811 the propagator. DMD can be viewed as the most direct generalization of this idea, as it explicitly forms
812 the empirical linear map without imposing an explicit stochastic model. Moreover, DMD admits a broad
813 range of generalizations - including extended DMD, kernel DMD, total-least-squares DMD, optimized
814 DMD, and control-aware variants - that relax linearity, incorporate noise and inputs, or approximate
815 Koopman operators on richer observable spaces, making it a more flexible framework in practice. For this
816 reason, we focus on DMD over the LIM or POP analysis as alternative methods. However, to keep the
817 analysis simple here, we will restrict ourselves to basic DMD.

818 Mathematically, DMD takes a sequence of state vectors $\mathbf{x}_1, \mathbf{x}_2, \dots, \mathbf{x}_k$, and seeks a matrix \mathbf{A} such that

819
$$\mathbf{x}_{j+1} \approx \mathbf{A} \mathbf{x}_j$$

820 for each time slice j . Equivalently, the state vectors are arranged into two data matrices: $\mathbf{X} = [\mathbf{x}_1, \mathbf{x}_2, \dots, \mathbf{x}_k]$
821 and $\mathbf{X}' = [\mathbf{x}_2, \mathbf{x}_3, \dots, \mathbf{x}_{k+1}]$. The matrix \mathbf{A} is then estimated by solving the linear system $\mathbf{X}' \approx \mathbf{A} \mathbf{X}$, often

822 using a low-rank approximation via the SVD. The eigenvalues and eigenvectors of the matrix A (or its
 823 projection onto a reduced subspace) reveal the dynamic modes and their temporal behavior. The
 824 dynamics of each mode is controlled by powers of the (complex) eigenvalue. Each mode evolves
 825 exponentially in time, either oscillating, growing, or decaying, and the full spatiotemporal dynamics of
 826 the system are represented as a linear combination of these modes.

827 Each eigenvalue λ_k governs the temporal evolution of the associated mode k 'th. Concretely, this is
 828 determined as follows. First, the amplitudes are determined by solving a least squares problem that
 829 projects the initial state onto the DMD modes. This finds the optimal coefficients to reconstruct the
 830 starting condition as a linear combination of the modes. Writing $\lambda_k = r_k e^{i\theta_k}$, the magnitude r_k determines
 831 exponential growth or decay, while the phase θ_k sets an oscillation with frequency. Using this, a
 832 continuous-time generator $\mu_k = 1/(\Delta t) \cdot \log_{f_0}(\lambda_k) = \sigma_k + i\omega_k$ is estimated so that the k 'th mode evolves as
 833 $e^{\sigma_k t} \cos_{f_0}(\omega_k t)$. The product of each mode's amplitude and its exponential evolution gives the temporal
 834 behavior of that individual mode, and these are combined together to reconstruct the full dynamics across
 835 all time steps.

836 Whereas EOFs prioritize variance maximization and produce orthogonal spatial patterns, DMD focuses
 837 on uncovering temporal dynamics and typically results in non-orthogonal modes. Moreover, DMD does
 838 not rank modes by explained variance, but rather by dynamical significance, such as dominant
 839 frequencies or timescales. In this sense, DMD can be viewed as complementary to EOF analysis. While
 840 EOFs are optimal for compressing information, DMD is better suited for analyzing and predicting time-
 841 evolving structures, especially in systems governed by approximately linear dynamics. Under many
 842 circumstances, DMD is equivalent to the well known method in the climate community known as **Linear**
 843 **Inverse Modeling (LIM)**⁵². The applications of LIM, and therefore DMD are quite vast across the Earth
 844 sciences, and it would be challenging to succinctly summarize its applications. We also note that DMD
 845 belongs to a broader class of algorithms, each designed to address different limitations of the traditional
 846 DMD framework, and ranging from mode collapse and scalability to improved representation of the

847 underlying dynamics⁵⁴. Given the limitations of this manuscript, we will not go into further descriptions
848 of these techniques.

849 **Extracted Structure and Applicability** - Dynamic Mode Decomposition isolates spatiotemporal modes
850 associated with approximately linear evolution, each characterized by a fixed frequency and growth or
851 decay rate. This makes coherent oscillatory behavior, traveling structures, and dominant timescales
852 explicit in both space and time, rather than prioritizing variance alone. DMD is most useful when the
853 dynamics can be well approximated by linear evolution over the sampling window, and when temporal
854 coherence or prediction is of primary interest. However, the method can be sensitive to noise, sampling,
855 and rank truncation, produces non-orthogonal modes, and may struggle to represent strongly nonlinear or
856 transient dynamics without extensions.

857 Techniques: Multi-Linear Methods

858 EOF analysis is traditionally applied to two-dimensional data matrices, such as a space \times time dataset.
859 However, many modern datasets are **multidimensional** (or *multilinear*): For example: latitude \times
860 longitude \times time; or: model ensemble \times latitude \times longitude \times time. Flattening these into a 2D matrix for
861 EOF analysis can destroy important structure — such as the difference between the two spatial
862 dimensions or between models and physical space.

863 Multilinear methods generalize the logic of EOFs to **tensors** — higher-order arrays — in ways that
864 preserve the multidimensional structure of the data. Rather than vectorizing or slicing the data and losing
865 directional specificity, multilinear decompositions seek to jointly decompose the full tensor along all its
866 modes. This enables mode-specific dimensionality reduction, where distinct sets of latent factors are
867 extracted along each axis (e.g., spatial modes, temporal modes, ensemble modes).

868 There are many different types of tensor decompositions, each with their own strengths and weaknesses.

869 Here we will cover two methods: **The Polyadic Decomposition**, also called

870 CANDECOMP/PARAFAC^{55,56} which generalizes a rank decomposition of a matrix, and the Tucker
 871 Decomposition⁵⁷, which generalizes PCA through a smaller core tensor.

872 Technique - Multilinear Methods: Polyadic Decomposition

873 **Canonical Polyadic Decomposition (CPD)** — also called CANDECOMP/PARAFAC — is a
 874 generalization of EOF analysis to higher-dimensional arrays, called tensors. If we combine the singular
 875 values with the PCs from EOFs, we can write

876
$$\mathbf{X} \approx \sum \mathbf{u}_r \mathbf{v}_r^T = \sum \mathbf{u}_r \otimes \mathbf{v}_r$$

877 Here, the \otimes symbol represents the **outer product** — a generalization of multiplication between vectors
 878 to form higher-dimensional arrays. Each term in the above sum has rank-1, and taking R singular vectors
 879 is a rank- R decomposition of \mathbf{X} . The outer product can be performed with more vectors to create higher
 880 dimensional arrays (tensors). CP does the same with rank-1 tensors in three or more dimensions.

881 Just as EOF expresses a 2D matrix as a sum of outer products of spatial and temporal modes, CP
 882 expresses a 3D (or 4D, 5D, etc.) data tensor as a sum of rank-1 tensors, each constructed from one vector
 883 in each dimension:

884
$$\mathbf{X} \approx \sum \mathbf{u}_r \otimes \mathbf{v}_r \otimes \mathbf{w}_r$$

885 This means that the data value at position (i, j, k) — say, (latitude i , longitude j , time k) — is
 886 approximated as a sum of products of values from: a spatial mode along dimension 1 (\mathbf{u}_r), a spatial mode
 887 along dimension 2 (\mathbf{v}_r), and a temporal mode (\mathbf{w}_r). Each term in the sum is like a triple-mode EOF
 888 component, one per mode of the data tensor. The number of such terms, R , is called the tensor rank, and it
 889 plays the same role as the number of retained EOFs: higher R captures more structure at the cost of
 890 increased complexity⁵⁸. In general, tensors can have as many dimensions as needed, allowing for
 891 complex interactions and large compression.

892 The CP decomposition expresses a tensor as a sum of \mathbf{R} separable components—one for each mode. This
 893 often leads to more parsimonious representations, particularly when the true structure of the data is
 894 separable across dimensions. Unlike EOFs, which discard tensor structure through matricization, CP
 895 preserves the full multidimensional nature of the data. While EOF modes are orthogonal by construction,
 896 CP components are not, yet the CP decomposition can still be unique under mild conditions, up to scaling
 897 and permutation⁵⁹. Moreover, CP yields mode-specific components (e.g., one temporal and two spatial),
 898 which can result in better physical interpretability.

899 **Extracted Structure and Applicability** - Canonical Polyadic Decomposition isolates separable, rank-1
 900 components across each mode of a multidimensional data tensor, yielding coupled spatial and temporal
 901 factors without flattening the data. This preserves the inherent multilinear structure and makes
 902 interactions across dimensions explicit, often resulting in parsimonious and physically interpretable
 903 representations. CP is most useful when the underlying processes are approximately separable across
 904 dimensions and when maintaining tensor structure is essential. However, the decomposition can be
 905 sensitive to noise and rank selection, lacks orthogonality, and may struggle to represent strongly non-
 906 separable or highly complex dynamics without increasing rank substantially.

907

908 Technique - Multilinear Methods: Tucker Decomposition

909 The **Tucker decomposition** generalizes EOF analysis to higher-order data arrays, or tensors, by allowing
 910 a low-rank projection along each dimension of the data simultaneously. Given a three-dimensional data
 911 tensor $\mathcal{X} \in \mathbb{R}^{\{I \times J \times K\}}$, such as latitude \times longitude \times time, Tucker approximates the data as:

$$912 \quad \mathcal{X} \approx \mathcal{G} \times_1 \mathbf{A} \times_2 \mathbf{B} \times_3 \mathbf{C}$$

913 Here, \mathbf{A} , \mathbf{B} , and \mathbf{C} are factor matrices containing the principal components along the first, second, and
 914 third modes, respectively—analogueous to the left and right singular matrices \mathbf{U} and \mathbf{V} matrices in SVD.

915 The core tensor $\mathcal{G} \in \mathbb{R}^{\{R_1 \times R_2 \times R_3\}}$ captures the interaction strengths between components from each

916 mode. The mode- n product \times_n represents a generalization of matrix multiplication to tensors, allowing us
917 to project \mathcal{X} along each axis independently⁵⁸.

918 Where EOFs decompose a matrix into rank-one outer products of vectors, Tucker decomposes a tensor
919 into a multilinear product of basis vectors and a dense core. The EOF decomposition can be viewed as a
920 special case of Tucker where the core tensor is diagonal and only two modes are present. Tucker relaxes
921 the orthogonality and diagonal structure, allowing for richer cross-mode interactions. The number of
922 components can be controlled independently for each axis, enabling anisotropic compression and a more
923 tailored approximation of the data.

924 **Extracted Structure and Applicability** - Tucker decomposition isolates low-dimensional subspaces
925 along each mode of a data tensor while explicitly modeling their interactions through a dense core tensor.
926 This makes cross-mode coupling and anisotropic structure visible, allowing different levels of
927 compression along space, time, or other dimensions. Tucker is most useful when variability is not well
928 captured by separable rank-1 components and when different modes exhibit distinct intrinsic
929 dimensionalities, or when the user needs to investigate more nuanced interactions between dimensions.
930 However, the core tensor can be difficult to interpret physically, the decomposition is not unique, and the
931 increased flexibility can lead to overfitting or reduced interpretability without careful rank selection.

932 Techniques: Direct Adjustment Methods

933 Methods that directly adjust sign flipping are automatically applied within Climate Variability
934 Diagnostics Package, version 6, (CVDPv6)¹⁷ and PCMDI Metrics Package (PMP)¹⁹ packages. In the
935 CVDPv6, the sign at a point in the center of action is used to determine whether the sign is consistent or
936 not, whereas for the PMP, a pattern correlation is used. PMP identifies the need of sign flipping by spatial
937 pattern correlation to the EOF pattern obtained from the reference dataset and flips the sign of the model's
938 pattern when the pattern correlation is negative. Additional diagnoses were applied for some variability
939 modes by assessing sign of area-averaged EOF pattern over certain geographical regions.

940

941 Mode swapping, however, is not automatically adjusted within the packages and is incumbent upon the
942 user to adjust manually. For example, one could use the statistics for determining mode swapping
943 described in section *Challenges with EOFs/Mode Swap*, and then manually change the mode numbers
944 assigned to the modes of interest (i.e. PSA1, PSA2). Table 1 mode swapping statistics were computed as
945 follows: We determine the absolute value of the pattern correlation between ERA5 PSA1 and a given
946 model and member's PSA1 and PSA2. Then, if the absolute value of the pattern correlation between
947 ERA5 PSA1 and the model's PSA2 is greater than the absolute value of the pattern correlation between
948 ERA5 PSA1 and model PSA1, we conclude that the modes are swapped. The forced response is
949 computed as the ensemble mean sea level pressure (SLP), which is removed from the SLP field prior to
950 calculation of the PSA1 and 2 modes. For observations, we use the 30-year running mean to define the
951 forced response, and that is also removed from PSL prior to calculation of the modes. Because mode
952 swapping is an artifact of statistical methods, frequency metrics (Table 1) can easily change due to
953 sampling. Examples of sampling choices include (but not limited to) detrending method, pattern
954 correlation methodology, time period used, ensemble set, number of ensemble members, etc.

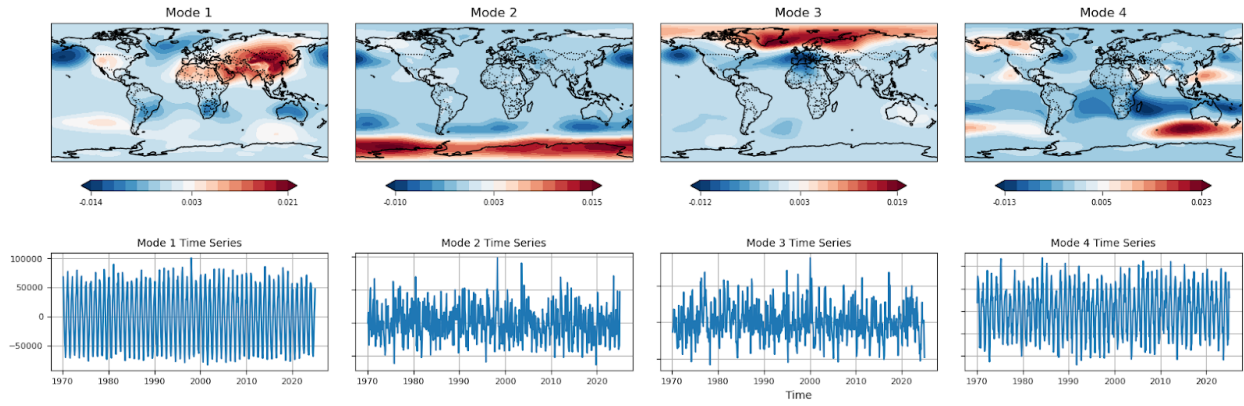
955

956 **Appendix**

957 For completeness and to provide illustrations of alternative methods discussed, we provide comparisons
958 with Figure 6's standard monthly PSL EOF, but for methods not shown in the *Alternative Method*
959 *Comparisons* section.

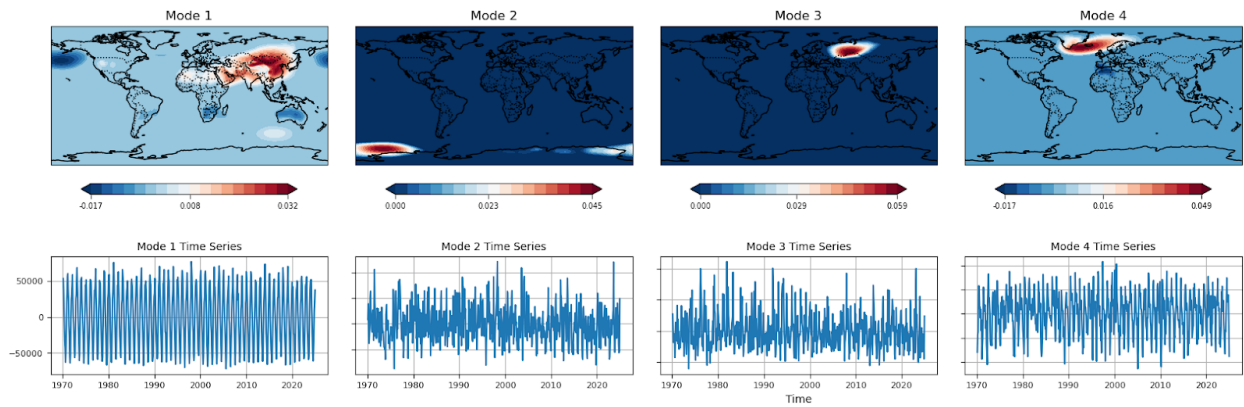
960 *Sparse EOFs*

961 Sparse EOFs were implemented using scikit-learn's MiniBatchSparsePCA algorithm. We present results
962 for varying values of the sparsity parameter α , with larger values enforcing greater sparsity. Specifically,
963 we examine $\alpha = 1000, 7000, \text{ and } 10000$.



964

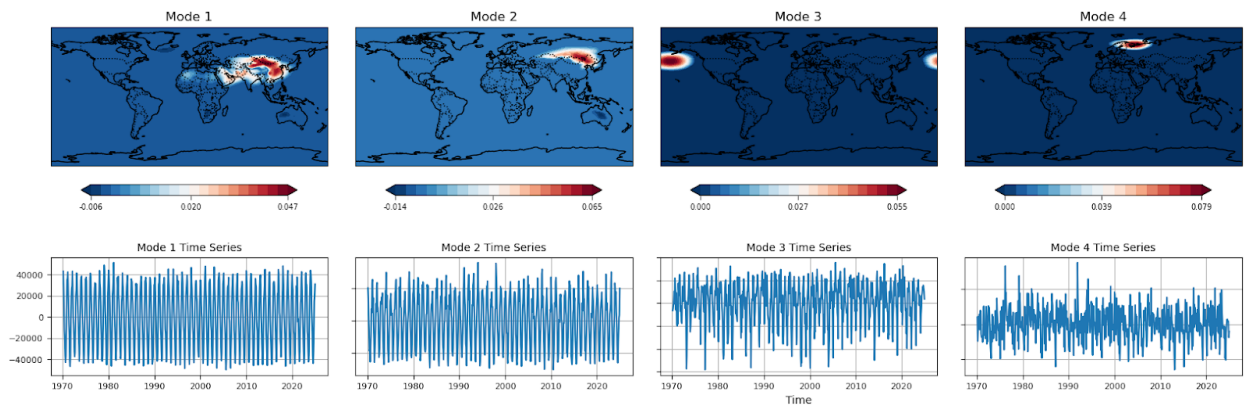
965 Figure A1. As in Figure 6, but an example of Sparse EOF, where $\alpha = 1000$.



966

967 Figure A2. As in Figure A1, but an example of Sparse EOF, where $\alpha = 7000$.

968



969

970 Figure A3. As in Figure A1, but an example of Sparse EOF, where $\alpha = 10000$.

971

972 For lower α , the spatial patterns closely resemble those from standard EOFs, with notable differences
 973 emerging primarily near regions of high variance, such as over Russia. As α increases, the modes become
 974 increasingly localized, concentrating around the primary centers of activity for each pattern. This spatial
 975 separation is reflected in the associated principal component time series, which begin to exhibit clearer
 976 seasonal structure, similar to that of the leading EOF mode.

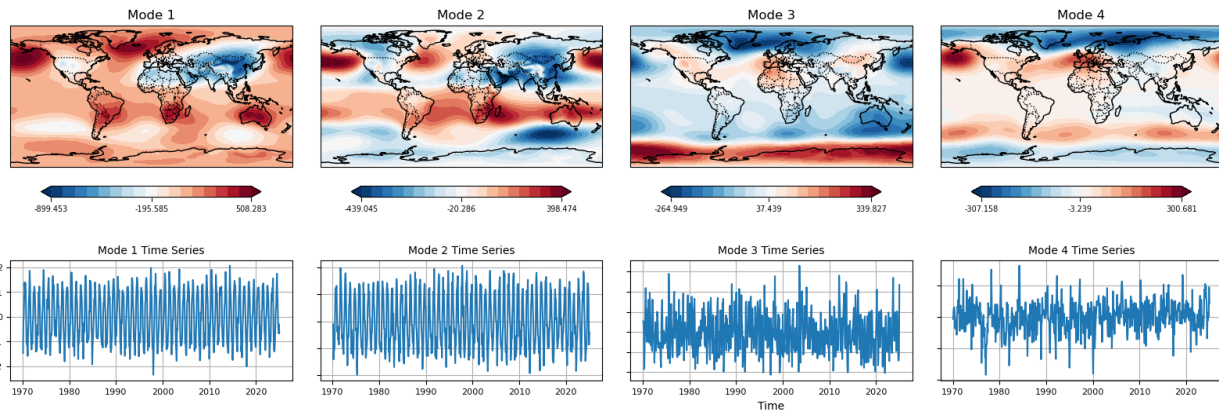
977

978 *Independent Component Analysis*

979 In ICA, the first mode appears quite similar to the first EOF. This means that the direction of maximal
 980 variance happens to also be the direction chosen to maximize independence. The second ICA mode is a
 981 large southern global teleconnection with nodes of importance in the Pacific and Atlantic. This appears to
 982 be a combination of the second and fourth EOFs. The third and fourth ICA modes grab the Southern and
 983 Northern Hemispheric patterns, analogous with the second and third EOFs.

984

985



986

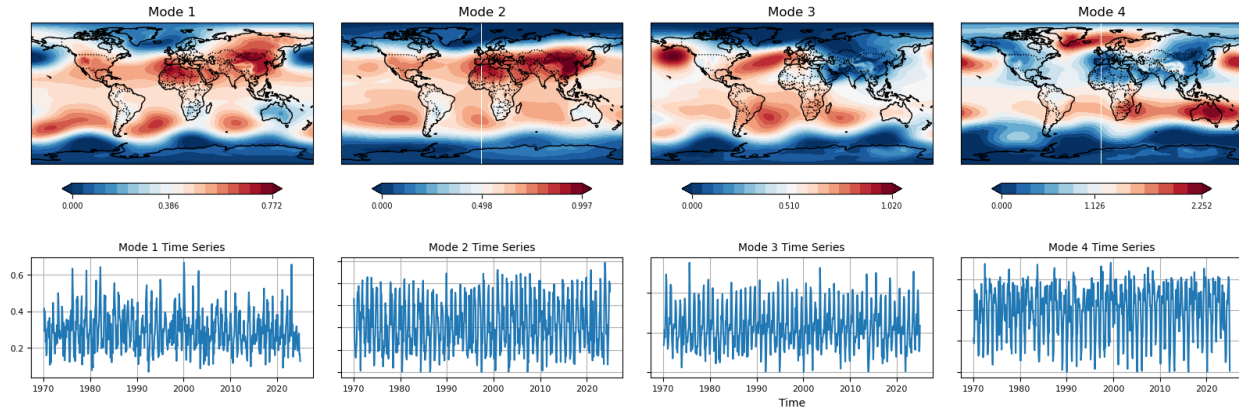
987 Figure A4. As in Figure 6, but for Independent Component Analysis

988

989 *Nonnegative Matrix Factorization*

990 In NMF, both the spatial and temporal modes are constrained to be nonnegative. The first two modes
 991 resemble those from the leading EOF, capturing the prominent Africa–South Asia signal. Subsequent

992 modes highlight other localized features, such as activity near Alaska and the North Atlantic. A key
 993 distinction of NMF, relative to other methods, is that the polar regions consistently remain near zero
 994 across all modes. This arises from the additive nature of NMF: unlike EOFs or other linear methods, it
 995 cannot balance large positive contributions with offsetting negative values. As a result, the decomposition
 996 emphasizes localized, purely additive structures, leading to inherently different spatial representations.



997

998 Figure A5. As in Figure 6, but for Nonnegative Matrix Factorization.

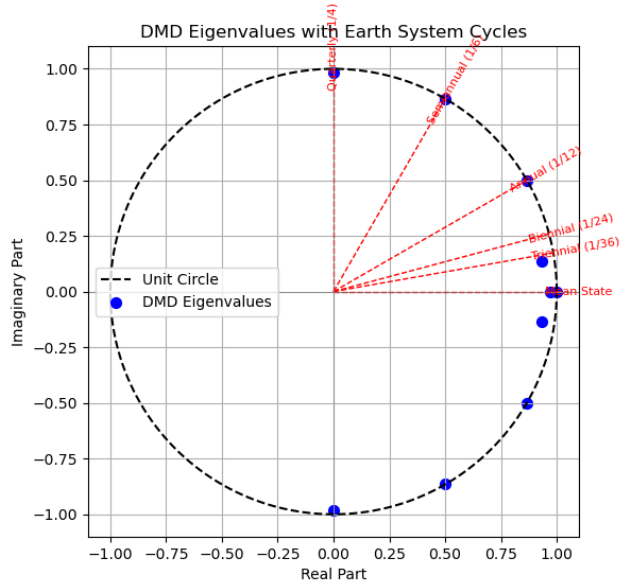
999

1000 *Dynamic Mode Decomposition*

1001 In the basic DMD algorithm, both spatiotemporal modes and their associated eigenvalues are extracted,
 1002 with both quantities generally complex-valued. The temporal evolution of each mode is governed by
 1003 powers of its corresponding eigenvalue, enabling fast and interpretable reconstruction of dynamics.

1004 Figure A6 is a plot of the leading eigenvalues, sorted by magnitude.

1005



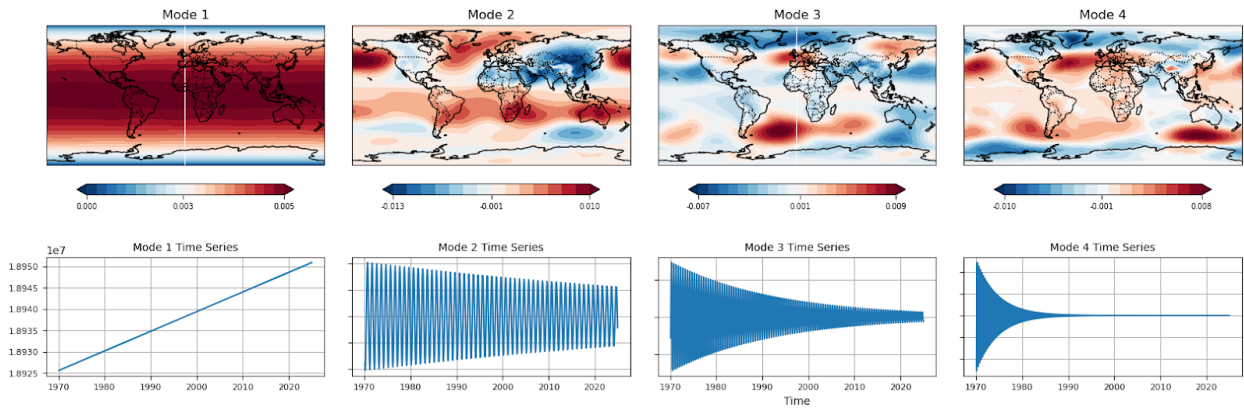
1006

1007 Figure A6. Leading eigenvalue with Earth System Cycles (mean state, triennial, biennial, annual,
 1008 semiannual, quarterly) sorted by magnitude. Blue circles represent DMD eigenvalues and the black
 1009 dashed line is a unit circle for reference.

1010

1011 To visualize the spatial patterns and dynamics, it is common practice to take the real parts of the modes
 1012 and time series. Since DMD eigenvalues often come in complex-conjugate pairs, care must be taken to
 1013 avoid redundancy by selecting only one representative from each pair. Shown here are the first four
 1014 distinct modes in Figure A7.

1015



1016

1017 Figure A7: As in Figure 6, but for dynamic mode decomposition.

1018

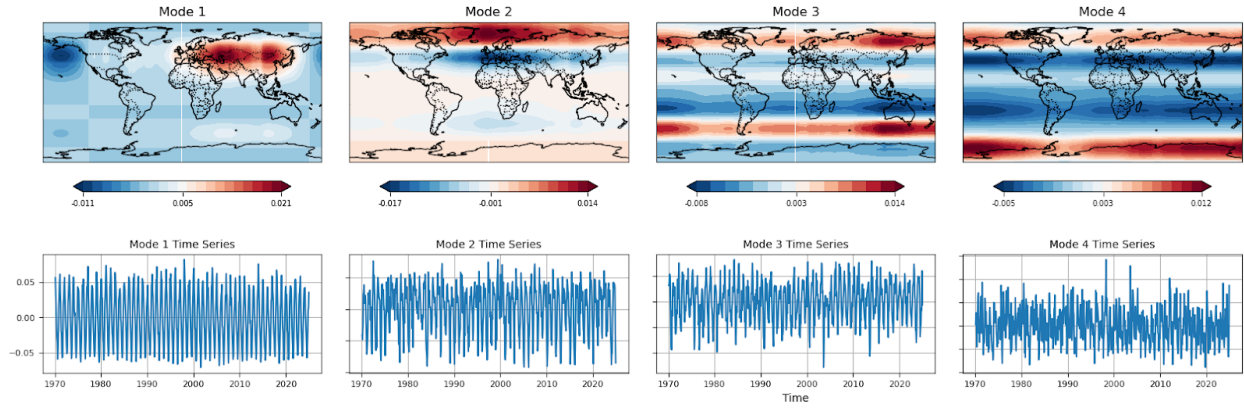
1019 From the structure of the eigenvalues, we identify these modes as corresponding to the mean, annual,
1020 semiannual, and quarterly cycles. The magnitude of each eigenvalue determines its long-term behavior:
1021 eigenvalues with magnitude one produce persistent oscillations; those less than one decay over time; and
1022 those greater than one amplify. In this case, the mean mode has a magnitude greater than one, suggesting
1023 a long-term warming trend. Indeed, the largest eigenvalue is $\lambda = 1.0000008+0i$ which is why we see 1) no
1024 oscillations and 2) slight growth. Decaying modes identified by DMD may reflect genuine physical
1025 transients or damping processes, but they can also arise as an artifact of extrapolating eigenvalues with
1026 magnitude less than one beyond the training interval. For example, a decaying seasonal mode might
1027 suggest a reduction in seasonal variability; however, standard DMD cannot substantiate this interpretation
1028 because it assumes time-independent growth rates over the entire analysis period. Windowed approaches
1029 or more advanced variants of DMD are required to distinguish true temporal evolution from such
1030 methodological artifacts.

1031

1032 *Canonical Polyadic Decomposition*

1033 In the CPD, we extract R modes along the latitude, longitude, and temporal dimensions, where R is the
1034 chosen decomposition rank. The spatial modes are formed by the outer product of the corresponding
1035 latitude and longitude factors, which we display below. The resulting spatial and temporal structures are
1036 highly sensitive to the choice of R. For low rank (e.g., R=4), the leading CPD modes resemble those from
1037 EOF analysis, with some notable distinctions. Specifically, the first CPD mode closely matches the
1038 leading EOF, while the others reflect the dataset's latitudinal structure, analogous to the second and third
1039 EOFs.

1040



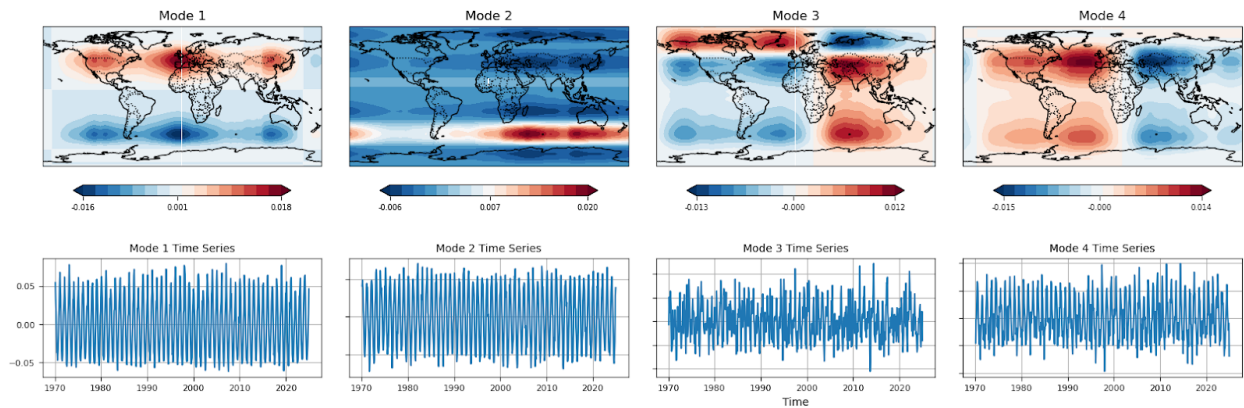
1041

1042 Figure A8. As in Figure 6, but for canonical polyadic decomposition using a low rank of $R=4$.

1043

1044 When the rank is increased (e.g., $R=12$), the decomposition reveals more complex structures. These
 1045 higher-rank modes tend to exhibit dipole-like or blocky spatial patterns not seen in the lower-rank or EOF
 1046 results. As CPD lacks a natural ordering of modes, we present a representative subset of these patterns in
 1047 Figure A9.

1048



1049

1050 Figure A9. As in Figure 6, but for canonical polyadic decomposition using a high rank of $R=12$.

1051

1052

1053 **References**

- 1054 1. Penland, C., and T. Magorian, 1993: Prediction of Niño 3 Sea Surface Temperatures Using
1055 Linear Inverse Modeling. *J. Climate*, 6, 1067–1076, [https://doi-](https://doi-org.cuucar.idm.oclc.org/10.1175/1520-0442(1993)006<1067:PONSST>2.0.CO;2)
1056 [org.cuucar.idm.oclc.org/10.1175/1520-0442\(1993\)006<1067:PONSST>2.0.CO;2](https://doi-org.cuucar.idm.oclc.org/10.1175/1520-0442(1993)006<1067:PONSST>2.0.CO;2).
- 1057 2. Lorenz EN (1956) Empirical orthogonal functions and statistical weather prediction. Statistical
1058 Forecasting Project report 1, MIT Department of Meteorology.
- 1059 3. North, G. R., T. L. Bell, R. F. Cahalan, and F. J. Moeng, 1982: Sampling Errors in the Estimation
1060 of Empirical Orthogonal Functions. *Mon. Wea. Rev.*, 110, 699–706, [https://doi-](https://doi-org.cuucar.idm.oclc.org/10.1175/1520-0493(1982)110<0699:SEITEO>2.0.C)
1061 [org.cuucar.idm.oclc.org/10.1175/1520-0493\(1982\)110<0699:SEITEO>2.0.C](https://doi-org.cuucar.idm.oclc.org/10.1175/1520-0493(1982)110<0699:SEITEO>2.0.C)
- 1062 4. von Storch H, Zwiers FW (1999) Statistical analysis in climate research. Cambridge University
1063 Press, Cambridge (ISBN: 0 521 45071 3).
- 1064 5. Hannachi A, Jolliffe IT, Stephenson DB (2007) Empirical orthogonal functions and related
1065 techniques in atmospheric science: a review. *Int J Climatol* 27:1119–1152.
- 1066 6. Monahan AH, Fyfe JC, Ambaum MH, Stephenson DB, North GR (2009) Empirical orthogonal
1067 functions: the medium is the message. *J Clim* 22:6501–6514.
- 1068 7. Chen, Z., B. Gan, L. Wu, and F. Jia, 2018: Pacific–North American teleconnection and North
1069 Pacific Oscillation: Historical simulation and future projection in CMIP5 models. *Climate Dyn.*,
1070 50, 4379–4403, <https://doi.org/10.1007/s00382-017-3881-9>.
- 1071 8. Lee, J., Sperber, K.R., Gleckler, P.J. et al. Quantifying the agreement between observed and
1072 simulated extratropical modes of interannual variability. *Clim Dyn* 52, 4057–4089 (2019).
1073 <https://doi-org.cuucar.idm.oclc.org/10.1007/s00382-018-4355-4>.
- 1074 9. Fasullo, J. T., A. S. Phillips, and C. Deser, 2020: Evaluation of Leading Modes of Climate
1075 Variability in the CMIP Archives. *J. Climate*, 33, 5527–5545, <https://doi.org/10.1175/JCLI-D-19->
1076 1024.1.

- 1077 10. Lian, T., and D. Chen, 2012: An Evaluation of Rotated EOF Analysis and Its Application to
1078 Tropical Pacific SST Variability. *J. Climate*, 25, 5361–5373, [https://doi.org/10.1175/JCLI-D-11-](https://doi.org/10.1175/JCLI-D-11-00663.1)
1079 [00663.1](https://doi.org/10.1175/JCLI-D-11-00663.1).
- 1080 11. Chen, X., J. M. Wallace, and K. Tung, 2017: Pairwise-Rotated EOFs of Global SST. *J. Climate*,
1081 30, 5473–5489, <https://doi.org/10.1175/JCLI-D-16-0786.1>.
- 1082 12. National Center for Atmospheric Research Staff (Eds). Last modified 22 Jul 2013. "The Climate
1083 Data Guide: Empirical Orthogonal Function (EOF) Analysis and Rotated EOF Analysis."
1084 Retrieved from [https://climatedataguide.ucar.edu/climate-data-tools-and-analysis/empirical-](https://climatedataguide.ucar.edu/climate-data-tools-and-analysis/empirical-orthogonal-function-eof-analysis-and-rotated-eof-analysis)
1085 [orthogonal-function-eof-analysis-and-rotated-eof-analysis](https://climatedataguide.ucar.edu/climate-data-tools-and-analysis/empirical-orthogonal-function-eof-analysis-and-rotated-eof-analysis).
- 1086 13. Weidman, S., Kleiner, N., & Kuang, Z. (2022). A rotation procedure to improve seasonally
1087 varying empirical orthogonal function bases for MJO indices. *Geophysical Research Letters*,
1088 49(15), e2022GL099998.
- 1089 14. Kay, J. E., and Coauthors, 2015: The Community Earth System Model (CESM) Large Ensemble
1090 Project: A Community Resource for Studying Climate Change in the Presence of Internal Climate
1091 Variability. *Bull. Amer. Meteor. Soc.*, 96, 1333–1349, [https://doi.org/10.1175/BAMS-D-13-](https://doi.org/10.1175/BAMS-D-13-00255.1)
1092 [00255.1](https://doi.org/10.1175/BAMS-D-13-00255.1).
- 1093 15. Milinski, S., Maher, N., and Olonscheck, D.: How large does a large ensemble need to be?, *Earth*
1094 *Syst. Dynam.*, 11, 885–901, <https://doi.org/10.5194/esd-11-885-2020>, 2020.
- 1095 16. Fasullo, J. T., and Coauthors, 2024: Modes of Variability in E3SM and CESM Large Ensembles.
1096 *J. Climate*, 37, 2629–2653, <https://doi.org/10.1175/JCLI-D-23-0454.1>.
- 1097 17. Phillips, A. S., C. Deser, and J. Fasullo, 2014: A New Tool for Evaluating Modes of Variability
1098 in Climate Models. *EOS*, 95, 453-455, doi: 10.1002/2014EO490002.
- 1099 18. Maher, N., Phillips, A. S., Deser, C., Wills, R. C. J., Lehner, F., Fasullo, J., Caron, J. M.,
1100 Brunner, L., and Beyerle, U.: The updated Multi-Model Large Ensemble Archive and the Climate
1101 Variability Diagnostics Package: New tools for the study of climate variability and change,
1102 *EGUsphere* [preprint], <https://doi.org/10.5194/egusphere-2024-3684>, 2024.

- 1103 19. Lee, J., Gleckler, P. J., Ahn, M.-S., Ordonez, A., Ullrich, P. A., Sperber, K. R., Taylor, K. E.,
1104 Planton, Y. Y., Guilyardi, E., Durack, P., Bonfils, C., Zelinka, M. D., Chao, L.-W., Dong, B.,
1105 Doutriaux, C., Zhang, C., Vo, T., Boutte, J., Wehner, M. F., Pendergrass, A. G., Kim, D., Xue, Z.,
1106 Wittenberg, A. T., and Krasting, J.: Systematic and objective evaluation of Earth system models:
1107 PCMDI Metrics Package (PMP) version 3, *Geosci. Model Dev.*, 17, 3919–3948,
1108 <https://doi.org/10.5194/gmd-17-3919-2024>, 2024.
- 1109 20. Dommenges, D. Evaluating EOF modes against a stochastic null hypothesis. *Clim Dyn* 28, 517–
1110 531 (2007). <https://doi.org/10.1007/s00382-006-0195-8>.
- 1111 21. Dommenges, D., & Latif, M. (2002). A cautionary note on the interpretation of EOFs. *Journal of*
1112 *Climate*, 15, 216–225.
- 1113 22. Kurihana, T., and Coauthors, 2024: Identifying Climate Patterns Using Clustering Autoencoder
1114 Techniques. *Artif. Intell. Earth Syst.*, 3, e230035, <https://doi.org/10.1175/AIES-D-23-0035.1>.
- 1115 23. Wills, R.C. J., Deser, C., McKinnon, K.A. et al. Forced Component Estimation Statistical Method
1116 Intercomparison Project (ForceSMIP). ESS Open Archive . June 16, 2025. DOI:
1117 10.22541/essoar.175003371.14843115/v1 .
- 1118 24. Zhang Y, Wallace JM, Battisti DS (1997) ENSO-like interdecadal variability: 1900–93’s. *J Clim*
1119 10:1004–1020.
- 1120 25. Bonfils C, Santer BD (2011) Investigating the possibility of a human component in various
1121 Pacific Decadal Oscillation indices. *Clim Dyn* 37:1457–1468. [https://doi.org/10.1007/s00382-](https://doi.org/10.1007/s00382-010-0920-1)
1122 [010-0920-1](https://doi.org/10.1007/s00382-010-0920-1).
- 1123 26. Bonfils C, Santer BD, Phillips TJ, Marvel K, Ruby Leung L, Doutriaux C, Capotondi A (2015)
1124 Relative contributions of mean-state shifts and ENSO-driven variability to precipitation changes
1125 in a warming climate. *J Clim* 28:9997–10013. <https://doi.org/10.1175/JCLI-D-15-0341.1>
- 1126 27. Hersbach H, Bell B, Berrisford P, et al. The ERA5 global reanalysis. *Q J R Meteorol Soc.* 2020;
1127 146: 1999–2049. <https://doi.org/10.1002/qj.3803>

- 1128 28. Compo, G.P., Whitaker, J.S., Sardeshmukh, P.D., Matsui, N., Allan, R.J., Yin, X., Gleason, B.E.,
1129 Vose, R.S., Rutledge, G., Bessemoulin, P., Brönnimann, S., Brunet, M., Crouthamel, R.I., Grant,
1130 A.N., Groisman, P.Y., Jones, P.D., Kruk, M.C., Kruger, A.C., Marshall, G.J., Maugeri, M., Mok,
1131 H.Y., Nordli, Ø., Ross, T.F., Trigo, R.M., Wang, X.L., Woodruff, S.D. and Worley, S.J. (2011),
1132 The Twentieth Century Reanalysis Project. *Q.J.R. Meteorol. Soc.*, 137: 1-28.
1133 <https://doi.org/10.1002/qj.776>
- 1134 29. Golaz, J.-C., Caldwell, P. M., Van Roekel, L. P., Petersen, M. R., Tang, Q., Wolfe, J. D., et al.
1135 (2019). The DOE E3SM coupled model version 1: Overview and evaluation at standard
1136 resolution. *Journal of Advances in Modeling Earth Systems*, 11, 2089–2129.
1137 <https://doi.org/10.1029/2018MS001603>
- 1138 30. Golaz, J.-C., Van Roekel, L. P., Zheng, X., Roberts, A. F., Wolfe, J. D., Lin, W., et al. (2022).
1139 The DOE E3SM Model version 2: Overview of the physical model and initial model evaluation.
1140 *Journal of Advances in Modeling Earth Systems*, 14, e2022MS003156.
1141 <https://doi.org/10.1029/2022MS003156>
- 1142 31. Hurrell, J. W., and Coauthors, 2013: The Community Earth System Model: A Framework for
1143 Collaborative Research. *Bull. Amer. Meteor. Soc.*, 94, 1339–1360,
1144 <https://doi.org/10.1175/BAMS-D-12-00121.1>.
- 1145 32. Danabasoglu, G., Lamarque, J.-F., Bacmeister, J., Bailey, D. A., DuVivier, A. K., Edwards, J., et
1146 al. (2020). The Community Earth System Model Version 2 (CESM2). *Journal of Advances in*
1147 *Modeling Earth Systems*, 12, e2019MS001916. <https://doi.org/10.1029/2019MS001916>
- 1148 33. Hannachi, A., Finke, K., & Trendafilov, N. (2023). Common EOFs: A tool for multi-model
1149 comparison and evaluation. *Climate Dynamics*, 60, 1689–1703. [https://doi.org/10.1007/s00382-](https://doi.org/10.1007/s00382-022-06409-8)
1150 [022-06409-8](https://doi.org/10.1007/s00382-022-06409-8).
- 1151 34. Flury, B. N. (1984). Common principal components in k groups. *Journal of the American*
1152 *Statistical Association*, 79, 892–898. <https://doi.org/10.2307/2288721>

- 1153 35. Lee, J., K. Sperber, P. Gleckler, K. Taylor, and C. Bonfils, 2021: Benchmarking performance
1154 changes in the simulation of extratropical modes of variability across CMIP generations. *Journal*
1155 *of Climate*, 34, 6945–6969, doi: 10.1175/JCLI-D-20-0832.1
- 1156 36. Richman, M. B. (1986). Rotation of principal components. *Journal of Climatology*, 6(3), 293–
1157 335. <https://doi.org/10.1002/joc.3370060305>
- 1158 37. Jolliffe, I. T. (2002). *Principal component analysis* (2nd ed.). Springer.
- 1159 38. Kaiser, H. F. (1958). The varimax criterion for analytic rotation in factor analysis. *Psychometrika*,
1160 23(3), 187–200. <https://doi.org/10.1007/BF02289233>
- 1161 39. Cheng, X., Nitsche, G., & Wallace, J. M. (1995). Robustness of low-frequency circulation
1162 patterns derived from EOF and rotated EOF analyses. *Journal of Climate*, 8, 1709–1713.
- 1163 40. Zou, H., Hastie, T., & Tibshirani, R. (2006). Sparse principal component analysis. *Journal of*
1164 *Computational and Graphical Statistics*, 15(2), 265–286.
1165 <https://doi.org/10.1198/106186006X113430>
- 1166 41. Witten, D. M., Tibshirani, R., & Hastie, T. (2009). A penalized matrix decomposition, with
1167 applications to sparse principal components and canonical correlation analysis. *Biostatistics*,
1168 10(3), 515–534. <https://doi.org/10.1093/biostatistics/kxp008>
- 1169 42. Weylandt, M., & Swiler, L. P. (2024). Beyond PCA: Additional dimension reduction techniques
1170 to consider in the development of climate fingerprints. *Journal of Climate*, 37(5), 1723–1735.
- 1171 43. Harman, H. H. (1976). *Modern factor analysis* (3rd ed.). University of Chicago Press.
- 1172 44. Kline, P. (1994). *An easy guide to factor analysis* (1st ed.). Routledge.
1173 <https://doi.org/10.4324/9781315788135>
- 1174 45. Hyvärinen, A., & Oja, E. (2000). Independent component analysis: Algorithms and applications.
1175 *Neural Networks*, 13(4–5), 411–430. [https://doi.org/10.1016/S0893-6080\(00\)00026-5](https://doi.org/10.1016/S0893-6080(00)00026-5).
- 1176 46. Forootan, E., Schumacher, M., Mehrnegar, N., Bezděk, A., Talpe, M. J., Farzaneh, S., ... & Shum,
1177 C. K. (2020). An iterative ICA-based reconstruction method to produce consistent time-variable
1178 total water storage fields using GRACE and Swarm satellite data. *Remote Sensing*, 12(10), 1639.

- 1179 47. Hannachi, A., Unkel, S., Trendafilov, N. T., & Jolliffe, I. T. (2009). Independent component
1180 analysis of climate data: A new look at EOF rotation. *Journal of Climate*, 22(11), 2797–2812.
- 1181 48. Lee, D. D., & Seung, H. S. (1999). Learning the parts of objects by non-negative matrix
1182 factorization. *Nature*, 401(6755), 788–791. <https://doi.org/10.1038/44565>
- 1183 49. Liang, C. S., Yue, D., Wu, H., Shi, J. S., & He, K. B. (2021). Source apportionment of
1184 atmospheric particle number concentrations with wide size range by nonnegative matrix
1185 factorization (NMF). *Environmental Pollution*, 289, 117846.
- 1186 50. Talsma, C. J., Bennett, K. E., & Vesselinov, V. V. (2022). Characterizing drought behavior in the
1187 Colorado River Basin using unsupervised machine learning. *Earth and Space Science*, 9(5),
1188 e2021EA002086.
- 1189 51. Schmid, P. J. (2010). Dynamic mode decomposition of numerical and experimental data. *Journal*
1190 *of Fluid Mechanics*, 656, 5–28. <https://doi.org/10.1017/S0022112010001217>
- 1191 52. Tu, J. H., Rowley, C. W., Luchtenburg, D. M., Brunton, S. L., & Kutz, J. N. (2014). On dynamic
1192 mode decomposition: Theory and applications. *Journal of Computational Dynamics*, 1(2), 391–
1193 421. <https://doi.org/10.3934/jcd.2014.1.391>
- 1194 53. Colbrook, M. J. (2024). The multiverse of dynamic mode decomposition algorithms. In
1195 *Handbook of Numerical Analysis* (Vol. 25, pp. 127–230). Elsevier.
- 1196 54. Schmid, P. J. (2022). Dynamic mode decomposition and its variants. *Annual Review of Fluid*
1197 *Mechanics*, 54(1), 225–254.
- 1198 55. Harshman, R.A., (1970). Foundations of the PARAFAC procedure: Models and conditions for an
1199 “explanatory” multi-modal factor analysis, UCLA Working Papers in Phonetics, 16 , pp. 1--84.
1200 Available online from <http://www.psychology.uwo.ca/faculty/harshman/wpppfac0.pdf>.
- 1201 56. Carroll, J. D. and Chang J.J., (1970). Analysis of individual differences in multidimensional
1202 scaling via an N-way generalization of “Eckart-Young” decomposition, *Psychometrika*, 35, pp.
1203 283--319, <https://doi.org/10.1007/BF02310791>.

- 1204 57. Tucker, L.R. Some mathematical notes on three-mode factor analysis. *Psychometrika* 31, 279–
1205 311 (1966). <https://doi.org/10.1007/BF02289464>.
- 1206 58. Kolda, T. G., & Bader, B. W. (2009). Tensor decompositions and applications. *SIAM Review*,
1207 *51*(3), 455–500. <https://doi.org/10.1137/07070111X>.
- 1208 59. Kruskal, J. B. (1977). Three-way arrays: Rank and uniqueness of trilinear decompositions. *Linear*
1209 *Algebra and Its Applications*, *18*(2), 95–138.

1210

1211 **Funding**

1212 CAS, JC, JF, and JL acknowledge support by the Regional and Global Model Analysis (RGMA)
1213 component of the Earth and Environmental System Modeling Program of the U.S. Department of
1214 Energy's Office of Biological & Environmental Research (BER) under (CAS, JC, JF) Lawrence
1215 Livermore National Lab subaward DE-AC52-07NA27344, Lawrence Berkeley National Lab subaward
1216 DE-AC02-05CH11231, and Pacific Northwest National Lab subaward DE-AC05-76RL01830. The work
1217 of JL is performed under the auspices of the U.S. Department of Energy (DOE) by Lawrence Livermore
1218 National Laboratory (LLNL) under Contract No. DE-AC52-07NA27344. AJ and DD were supported by
1219 the Regional and Global Model Analysis (RGMA) component of the Earth and Environmental System
1220 Modeling (EESM) program of the U.S. Department of Energy's Office of Science, as a contribution to the
1221 HiLAT-RASM project. The efforts of Dr. Fasullo in this work were also supported by NASA Awards
1222 80NSSC21K1191, 80NSSC17K0565, and 80NSSC22K0046. This work was supported by the National
1223 Center for Atmospheric Research, which is a major facility sponsored by the National Science Foundation
1224 (NSF) under Cooperative Agreement No. 1852977. Additionally, this research used resources of the
1225 National Energy Research Scientific Computing Center (NERSC), a U.S. Department of Energy Office of
1226 Science User Facility located at Lawrence Berkeley National Laboratory, operated under Contract No.
1227 DE-AC02-05CH11231 using NERSC award BER-ERCAP0033110.

1228

1229

1230 **Author contributions**

1231 CAS contributions include research inception and design, project management and organization, writing,
1232 and editing; DD writing, alternate method expertise, figure creation; AJ research inception and design,
1233 writing, figure creation; JL writing and figure creation; JC figure creation and statistics; AP figure
1234 creation; JF editing.

1235

1236 **Competing Interests**

1237 CAS is an Associate Editor for npj Climate and Atmospheric Sciences.

1238

1239 **Data availability**

1240 E3SMv2 Large Ensemble, 1850-2100,

1241 https://portal.nersc.gov/archive/home/c/ccsm/www/E3SMv2/FV1/atm/proc/tseries/month_1; CESM2

1242 Large Ensemble, 1950-2023, <https://www.earthsystemgrid.org/dataset/ucar.cgd.cesm2le.output.html>;

1243 E3SMv1 ensemble data, LLNL ESGF node, <https://aims2.llnl.gov/>; CESM1 Large ensemble, NSF

1244 NCAR Research Data Archive, <https://rda.ucar.edu/datasets/d651027/>; ERA5, 1950-2023, PSL

1245 <https://cds.climate.copernicus.eu/datasets/reanalysis-era5-single-levels-monthly-means?tab=overview>;

1246 The Twentieth Century Reanalysis (20CR), https://psl.noaa.gov/data/20thC_Rean/.

1247

1248 **Figure legends**

1249

1250 **Figure 1:** East Atlantic pattern (EA, row 1) and Scandinavian pattern (SCA, row 2) shown for ERA5

1251 (first column), CESM2 ScenarioMIP ensemble member r1i1p1f1 (second column) and CESM2

1252 ScenarioMIP ensemble member r3i1p1f1 (third column). Mode swapping is evident in the third column.

1253 EA and SCA are defined as the 2nd and 3rd EOF patterns of area-weighted PSL computed over 20:80°N,

1254 -90:40°E for JFM 1979-2022. Units are in hPa and variance explained is listed at the top right of each
1255 panel.

1256 **Figure 2:** Pacific South American (PSA) modes 1 (row 1) and 2 (row 2) shown for ERA5 (first column),
1257 CESM2 Large Ensemble member 1181.010 (second column) and CESM2 Large Ensemble member
1258 1161.009 (third column). Mode swapping is evident in the third column. PSA1 and PSA2 are defined as
1259 the 2nd and 3rd EOF patterns of area-weighted PSL computed over 20:90°S, 0:360°E for June-August
1260 1950-2023. Units are in hPa and variance explained is listed at the top right of each panel. The patterns
1261 are created by regressing global PSL anomalies onto normalized PC timeseries.

1262 **Figure 3:** Pacific North American pattern shown for ERA5 (first panel), E3SMv2 member r18i1p1f1
1263 (second panel) and E3SMv2 member r29i1p1f1 (third panel). Sign flipping is evident in the third panel.
1264 Units are in hPa and variance explained for each pattern is listed at the top right. The PNA is defined as
1265 the first EOF pattern of area-weighted PSL computed over 20:85°N, 120°E:120°W for June-August 1950-
1266 2022. Units are in hPa and variance explained is listed at the top right of each panel. The patterns are
1267 created by regressing global PSL anomalies onto normalized PC timeseries.

1268 **Figure 4:** Center of action variability for North Atlantic Oscillation (top), East Atlantic (middle) and
1269 Scandinavian (top) patterns computed for three ensemble members of the E3SMv2 Large Ensemble: 0101
1270 (left), 0201 (center), and 0301 (right), for a combination of historical and SSP370 simulations. The NAO
1271 is defined as the first EOF, the East Atlantic pattern as the second EOF and the Scandinavian pattern as
1272 the third EOF of area-weighted PSL computed over 20:80°N, 90°W:40°E for January-March over 100-
1273 year periods staggered by 10 years. The mean EOFs are shown, as well as the centers of action for each of
1274 the sixteen 100-year periods between 1850 and 2100, marked by white dots.

1275 **Figure 5.** Mode swapping pattern correlation adjustment method illustration. (Upper panel) Pattern
1276 correlation of CMIP6 models' Pacific/North American (PNA) pattern during the September-October-
1277 November (SON) season (upper panel). The PNA pattern for each model was determined by the leading
1278 Empirical Orthogonal Function (EOF 1) of sea level pressure fields. Pattern correlation was then
1279 calculated between each model's EOF 1 spatial pattern and the 20th Century Reanalysis (20CR) PNA

1280 pattern (SON season). For each model, the pattern correlation of the leading three EOFs (EOF 1-3) was
1281 assessed against the 20CR PNA using spatial pattern correlation, Root Mean Square Error (RMSE), and
1282 temporal correlation between the EOF principal component (PC) time series and a Common Basis
1283 Function PC time series. The highest pattern correlation achieved after potentially swapping EOF modes
1284 based on these criteria is indicated by markers, while the pattern correlation of the original EOF 1 is
1285 shown as a gray bar. The increasing spread between EOF1 and the alternative EOF on the right
1286 demonstrates the difficulty in automated selection of the best-matching EOF mode for models on the
1287 right, which highlights challenges in systematically identifying robust climate patterns across different
1288 models (further details in Lee et al., 2019). (Lower panel) Spatial pattern of model's EOF 1 (left), 2
1289 (middle) and reference dataset's EOF 1 demonstrating an example EOF swap case, obtained from EC-
1290 Earth3-AerChem model (far-most right in the upper panel) and the 20CR for PNA pattern during the SON
1291 season.

1292 **Figure 6.** Figure 6. PSL EOFs 1,2,3,4 (with percent variance explained) and respective PC timeseries for
1293 CESM2 model large ensemble, first member. No temporal filtering is done for consistency and
1294 comparison across alternative methods. See the Methods section under *EOF: Standard Computation* for
1295 an illustration on the potentially large differences due to temporal filtering.

1296 **Figure 7.** As in Figure 6, but an example of rotated EOF.

1297 **Figure 8.** As in Figure 6 but using Factor Analysis.

1298 **Figure 9.** Tucker decomposition core tensor of PSL CESM2 large ensemble member in Figure 6, with a
1299 multirank of (5, 10, 10), with temporal modes 0 through 4, 10 latitudes (y-axis) and 10 longitudes (x-
1300 axis).

1301 **Figure 10.** As in Figure 6, but for Tucker decomposition for the first four temporal components using the
1302 largest weights.

1303 **Figure 11.** As in Figure 9, except using all core weights in combination.

1304 **Figure 12.** As in Figure 6, except using a 1 year rolling average to demonstrate the potentially large
1305 differences when temporal filtering is applied.